THE ASTROPHYSICAL JOURNAL, 536:36–61, 2000 June 10

NICMOS IMAGING OF THE DAMPED Lyα ABSORBER AT $z = 1.89$ TOWARD LBQS 1210+1731: CONSTRAINTS ON SIZE AND STAR FORMATION RATE

VARSHA P. KULKARNI,[1] JOHN M. HILL, AND GLENN SCHNEIDER
University of Arizona, Steward Observatory, Tucson, AZ 85721

RAY J. WEYMANN AND LISA J. STORRIE-LOMBARDI[2]
Carnegie Observatories, Pasadena, CA 91101

MARCIA J. RIEKE AND RODGER I. THOMPSON
University of Arizona, Steward Observatory, Tucson, AZ 85721

AND

BUELL T. JANNUZI
National Optical Astronomy Observatories, P. O. Box 26732, Tucson, AZ 85726-6732
Received 1999 June 18; accepted 2000 January 20

ABSTRACT

We report results of a high-resolution imaging search for the galaxy associated with the damped Lyα (DLA) absorber at $z = 1.892$ toward the $z_{em} = 2.543$ quasar LBQS 1210+1731, using the *Hubble Space Telescope* (*HST*) NICMOS. The images were obtained in the broad filter F160W and the narrow filter F190N with camera 2 on NICMOS and were aimed at detecting the absorber in the rest-frame optical continuum and in Hα line emission from the DLA absorber. After suitable point-spread function (PSF) subtractions, a feature is seen in both the broadband and narrowband images, at a projected separation of 0.″25 from the quasar. This feature may be associated with the DLA absorber, although we cannot completely rule out that it could be a PSF artifact. If associated with the DLA, the object would be ≈ 2–$3\ h_{70}^{-1}$ kpc in size with a flux of 9.8 ± 2.4 μJy in the F160W filter, implying a luminosity at $\lambda_{central} = 5500$ Å in the rest frame of $1.5 \times 10^{10}\ h_{70}^{-2}\ L_{\odot}$ at $z = 1.89$, for $q_0 = 0.5$. However, a comparison of the fluxes in the broad and narrow filters indicates that most of the flux in the narrowband filter is continuum emission, rather than redshifted Hα line emission. This suggests that if this object is the absorber, then either it has a low star formation rate (SFR), with a 3 σ upper limit of $4.0\ h_{70}^{-2}\ M_{\odot}\ \mathrm{yr}^{-1}$, or dust obscuration is important. It is possible that the Hα emission may be extinguished by dust, but this seems unlikely, given the typically low dust-to-gas ratios observed in DLAs. Alternatively, the object, if real, may be associated with the host galaxy of the quasar rather than with the damped Lyα absorber. *H*-band images obtained with the NICMOS camera 2 coronagraph show a much fainter structure ≈ 4–$5\ h_{70}^{-1}$ kpc in size and containing four knots of continuum emission, located 0.″7 away from the quasar. This structure is not seen in images of comparison stars after similar PSF subtractions and is also likely to be associated with the absorbing galaxy or its companions, although we do not know its redshift. We have probed regions far closer to the quasar sight line than in most previous studies of high-redshift intervening DLAs. The two objects we report mark the closest detected high-redshift DLA candidates yet to any quasar sight line. If the features in our images are associated with the DLA, they suggest faint, compact, somewhat clumpy objects rather than large, well-formed protogalactic disks or spheroids. If the features are PSF artifacts, then the constraints on sizes and star formation rates of the DLA are even more severe. The size, luminosity, and SFR estimates mentioned above should therefore be conservatively considered as upper limits.

Subject headings: cosmology: observations — galaxies: evolution — infrared: galaxies — intergalactic medium — quasars: absorption lines

1. INTRODUCTION

Damped Lyα absorption systems detected in spectra of high-redshift quasars are believed to be the progenitors of present-day galaxies because they show high H I column densities ($\log N_{HI} \geq 20.0$) and display absorption lines of several heavy elements. However, there are various competing ideas regarding the nature of the galaxies underlying the DLAs. Wolfe et al. (1986) suggested that the DLAs are rotating protodisks. This suggestion has also been made by Prochaska & Wolfe (1997, 1998), based on asymmetric line profiles of the heavy-element absorption lines in DLAs. On the other hand, gas-rich dwarf galaxies have also been suggested as candidate objects for the DLAs (York et al. 1986; Matteucci, Molaro, & Vladilo 1997). Recently, Jimenez, Bowen, & Matteucci (1999) have suggested that high-redshift DLAs may arise in low-surface brightness galaxies. The lack of substantial chemical evolution found in studies of element abundances in DLAs (e.g., Pettini et al. 1999; Kulkarni et al. 1999) also shows that the currently known population of DLAs seems to be dominated by metal-poor objects, so DLAs may consist of dwarf or low surface brightness galaxies with modest star formation rates. Unfortunately, it is hard to determine what type of galaxies underlie the DLAs, since most previous efforts to directly image the high-redshift DLAs have failed. A few detections

[1] Present address: Clemson University, Department of Physics and Astronomy, Clemson, SC 29634.

[2] Present address: Space Infrared Telescope Facility Science Center, Caltech, Pasadena, CA 91125.

have been made at low redshifts, which showed those DLAs to arise in low surface brightness galaxies (see, e.g., Steidel et al. 1995a, 1995b; LeBrun et al. 1997). However, high-redshift DLAs with $z_{abs} < z_{em}$ have proven hard to detect, and the question of the nature of galaxies giving rise to these DLAs is still open.

Many of the previous attempts to detect the emission from DLAs concentrated on the Lyα emission, which is an expected signature from a star-forming region (e.g., Smith et al. 1989; Hunstead, Pettini, & Fletcher 1990; Lowenthal et al. 1995). There have been only a few Lyα detections of DLAs so far. Møller & Warren (1998) and Møller, Warren, & Fynbo (1998) detected Lyα emission in the fields of two DLAs at $z = 2.81$ and $z = 1.93$. However, both of these DLAs have $z_{abs} \approx z_{em}$ and may be different from the general population of intervening DLAs. Djorgovski et al. (1996) and Djorgovski (1997) reported Lyα-emitting objects with $R \sim 25$ (and inferred star formation rates [SFRs] of a few $M_\odot$ yr^{-1}) in fields of a few DLAs, located at 2″–3″ from the quasar. However, the Lyα technique cannot definitively measure the star formation rates of the DLAs because of the generally unquantifiable effects of dust extinction in the systems. The lack of detections in the other Lyα studies of intervening DLAs could indicate either that DLAs have low star formation rates (SFR) or that the emission is extinguished by dust. As pointed out by Charlot & Fall (1991), even small quantities of dust are sufficient to extinguish the Lyα emission, since resonant scattering greatly increases the path length of Lyα photons attempting to escape from an H I cloud. Indeed, observations of reddening of background quasars and evidence for depletion of Cr, Fe, Ni, etc., relative to Zn suggest the presence of a small amount of dust in DLAs (see, e.g., Pei, Fall, & Bechtold 1991; Pettini et al. 1997; Kulkarni, Fall, & Truran 1997). Thus, it is hard to constrain the SFRs in DLA galaxies using the nondetections or weak detections of Lyα emission.

The issues of dust and SFR in high redshift DLAs are also important in view of recent claims based on mid-IR and far-IR observations that a large fraction of the star formation at high redshifts is hidden from us by dust obscuration (e.g., Elbaz et al. 1998; Clements et al. 1999). One way to discern whether the previous nondetections of Lyα were due to low SFR or presence of dust is to search for longer wavelength emission lines less affected by dust extinction and not subject to resonant scattering. The ground-based near-IR spectroscopic survey of Bunker et al. (1999), which searched for redshifted Hα emission in 11″ × 2.″5 regions around six quasars with DLAs at $z > 2$ and reached 3 σ detection levels of 6–18 $M_\odot$ yr^{-1}, failed to detect any redshifted Hα emission from the DLAs in their sample. Some of the ground-based narrowband photometric surveys for Hα emission from DLAs have also failed to detect any emission line objects in the DLA fields (e.g., Teplitz, Malkan, & McLean 1998, who, however, found Hα emitters in the fields of some weaker non-DLA metal-line systems). Some other narrowband searches for Hα emission have revealed multiple objects in the DLA fields separated by several arcseconds from the quasar (2″–12″ for Bechtold et al. 1998; 9″–120″ for Mannucci et al. 1998). These surveys, which had 3 σ detection limits of $\sim 5\ M_\odot$ yr^{-1} (Bechtold et al. 1998) or $\gtrsim 10\ M_\odot$ yr^{-1} (Mannucci et al. 1998), found the Hα-emitting objects to have a wide range of inferred SFRs (10–20 $M_\odot$ yr^{-1} for Bechtold et al. 1998; 6–90 $M_\odot$ yr^{-1} for Mannucci et al. 1998). The relatively large separations of these emission-line objects from the quasars indicates that they are not the DLA absorbers themselves but star-forming companions in the same larger structure (e.g., sheet or filament) as the DLA. None of these ground-based surveys has been able to probe the regions very close to the quasar sight line (angular separations <2″) because of the limitations imposed by seeing in these studies. While these studies offer interesting information about the environments of the DLAs, high-sensitivity diffraction-limited imaging is necessary for the detection of the DLA absorbers themselves (to probe small angular separations), and thus for determining the morphology and SFRs of the DLAs. The *Hubble Space Telescope* (*HST*) WFPC2 study of Le Brun et al. (1997) has detected candidates with angular separations of less than 2″ in broadband images for six DLAs at $z < 1$ and one DLA at $z = 1.78$. However, the information obtained from this study about the nature of high-redshift DLAs is limited since no narrowband images were obtained and since the sample contained only one DLA at $z > 1$. As mentioned earlier, the *HST* WFPC2 study of Møller & Warren (1998, and references therein) detected Lyα emission in a $z_{abs} > z_{em}$ DLA, but this DLA may differ from intervening DLAs.

To summarize, many previous attempts to detect emission from high-redshift intervening DLAs have failed. The few detections so far consist mainly of either weak Lyα detections (which cannot constrain the SFR completely) or detections of Hα companions at fairly large angular separations from the quasars. There are only four objects detected so far in fields of high-z intervening DLAs at small angular separations. These objects have impact parameters between 4.3 and 11.5 h_{70}^{-1} kpc (where $H_0 = 70\ h_{70}$ km s^{-1} Mpc^{-1}) and are promising candidates for the DLAs in those sight lines (see Møller & Warren 1998 and references therein; the other DLA impact parameter data listed in Møller & Warren 1998 are biased toward $z_{abs} \approx z_{em}$ DLAs). To further increase the number of promising candidates for high-redshift intervening DLAs, it is necessary to carry out more deep high spatial resolution near-infrared searches for DLAs.

We have obtained deep diffraction-limited images of three DLAs at $z \sim 2$ with the Near Infrared Camera and Multi-Object Spectrometer (NICMOS) on board the *Hubble Space Telescope* (*HST*). Here we describe our NICMOS observations of the quasar LBQS 1210+1731 ($z_{em} = 2.543 \pm 0.005$; Hewett, Foltz, & Chaffee 1995), which has a spectroscopically known damped Lyα absorber ($z_{abs} = 1.8920$ and $\log N_{HI} = 20.6$; Wolfe et al. 1995). Our observations have the unique benefit of combining high near-IR sensitivity and high spatial resolution with a more stable and quantifiable point-spread function (PSF) than is currently possible with ground-based observations. A further feature of some of our observations is the use of the NICMOS coronagraph, which greatly decreases the scattered light background outside of the coronagraphic hole and therefore allows a study of the environment of the DLA. Our analysis indicates two objects at 0.″25 and 0.″7 from the quasar that we cannot explain as any known artifacts of the PSF. We believe that these objects are likely to be real and may be associated with the DLA and its companions, at impact parameters of 1.5 and 3.8 h_{70}^{-1} kpc. We have thus probed regions far closer to the quasar sight line than in most previous studies of high-redshift intervening DLAs, and the two objects we report mark the closest

detected high-redshift intervening DLA candidates yet to any quasar sight line. Sections 2, 3, and 4 describe the observations, data reduction, and the subtraction of the quasar point-spread functions. Our results are described in § 5. Section 6 describes various tests of our data analysis procedures, carried out to investigate whether the features seen after PSF subtraction are real. A summary of the results of the various data analysis tests is given in § 6.12. (Readers interested mainly in the scientific discussion can go directly from § 5 to § 6.12.) Finally, §§ 7 and 8 discuss the implications of our observations for sizes, environment, and star formation rates of DLA galaxies.

2. OBSERVATIONS

The field of LBQS 1210+1731 was first observed on 1998 July 22 from 07:14 to 16:40 UT, using NICMOS camera 2 (pixel scale $\approx 0\farcs076$, field of view $19\farcs45 \times 19\farcs27$). A sequence of spatially offset broadband images was obtained in MULTIACCUM mode with the F160W (H) filter (central wavelength 1.5940 μm, FWHM 0.4030 μm). Field offsetting was accomplished with a five-point spiral dither pattern in steps of ≈ 7.5 pixels, using the field offset mirror (FOM) internal to NICMOS. The exposures at each dwell point were 512 s long, giving a total integration time of 2560 s. See MacKenty et al. (1997) for a detailed description of NICMOS imaging modes and options. The MULTIACCUM observations consisted of nondestructive readouts in the STEP32 readout timing sequence, i.e., MULTIACCUM readouts separated logarithmically up to 32 s and linearly in steps of 32 s beyond that. In addition, narrowband images were obtained in the filter F190N (central wavelength 1.9005 μm, FWHM 0.0174 μm), in which the redshifted Hα emission from the DLA, if present, would lie. Four-point spiral dither patterns in steps of 7.5 pixels, with a 704 s STEP64 MULTIACCUM exposure at each dwell point, were repeated in five successive orbits, resulting in a total integration time of 14,080 s. The spatial resolution of the F160W and F190N images is $0\farcs14$ (1.8 pixels) and $0\farcs17$ (2.1 pixels) FWHM, respectively. Thus, camera 2 is almost critically sampled at the wavelengths used for our observations.

Finally, broadband images in the F160W filter were also obtained using the camera 2 coronagraph on 1998 July 29 from 10:14 to 13:07 UT. These consisted of an initial pair of 92 s long target-acquisition images, which were followed by placement of the target in the coronagraphic hole ($0\farcs3$, or 4 pixels in geometrical radius) and then integration of the object for a total of 4960 s (five exposures of 480 s each in the first orbit and five exposures of 512 s each in the second orbit, all using the STEP32 MULTIACCUM timing sequence). No dithering was used, of course, for the coronagraphic observations. The NICMOS coronagraph is comprised of two optical elements, a 165 μm physical diameter hole in the camera 2 field divider mirror at the reimaged *HST* f/24 optical telescope assembly (OTA) focus, and a Lyot stop at a cold pupil in the cryostat. The coronagraphic system significantly reduces both scattered and diffracted energy from the occulted target's point-spread function core by factors of 4–6 compared to direct imaging (Schneider et al. 1998; Lowrance et al. 1998). Thus, our coronagraphic images have higher sensitivity than the noncoronagraphic images for detecting those foreground damped Lyα absorber or associated companions that are much fainter than the quasar and lie outside the coronagraphic hole.

To circumvent image artifacts known as "bars" in all our camera 2 images, cameras 1 and 3 were run in parallel, as discussed by Storrs (1997).

3. REDUCTION OF IMAGES

The images were reduced using the IRAF package NICRED 1.8, developed specifically for the reduction of MULTIACCUM NICMOS data (McLeod 1997). The dark image used was that made from on-orbit dark exposures taken during the NICMOS calibration program. For the noncoronagraphic images, the flat-field image used was made from on-orbit exposures taken with the internal calibration lamps during the NICMOS Cycle 7 calibration program. For the coronagraphic images, the flat-field image was made with target-acquisition data taken just before the coronagraphic exposures. This ensures that the coronagraphic hole is in the same position on the detector for the flat as for the quasar data, which is critical for studying faint objects close to the edge of the coronagraphic hole. (The standard calibration flats are not adequate for this purpose because the position of the coronagraphic hole on the detector changed with time, and a flat exposure taken at another time had the hole in a different place.)

First, the exposures at each individual dither position were reduced using NICRED 1.8. Briefly, the steps followed by NICRED 1.8 are as described below:

1. subtraction of the zeroth read from successive reads, both for the quasar data and the dark data;
2. dark subtraction, read by read;
3. linearity correction, cosmic ray rejection, and fitting of slope to the successive reads in the multiaccum data, to get count rates in analog-to-digital converter units (ADU) s^{-1};
4. correction of nonuniform bias level across the array ("the pedestal effect");
5. repeating step 3 on the bias-corrected image to get more accurate count rates;
6. flat fielding using the appropriate flats;
7. subtracting the median of each row from that row and then likewise for columns, to remove bands caused by bias jumps during simultaneous use of amplifiers of other cameras in parallel, and thus to improve the flatness of the background;
8. fixing bad pixels using bicubic spline interpolation across the neighboring pixels.

The images for the different dither positions were registered by cross-correlating with the IRAF task XREGISTER. The quasar was used as the reference object since no other point sources were available in our images. Finally, the registered images were averaged together using a bad-pixel mask that took out any remaining bad pixels, and rejecting pixels deviating by more than 3 σ from the average of the five F160W images, using averaged sigma clipping.

For the F190N images, where there were five exposures (one in each orbit) at each of the four dither positions, we first median combined the five exposures at each position separately and then registered and median combined the four positions together to make the final image. For the coronagraphic F160W images, where there were five exposures at the same position in each of the two orbits, we averaged the exposures in each orbit separately and then took a weighted average (weighting by exposure times) of the combined exposures from the two orbits.

In an attempt to gain the higher spatial resolution made possible by the half-integral pixel dithers (in steps of 7.5 pixels), we also experimented with magnification (repixelization) of the images at the individual dither positions before combining them. The images for each individual dither position processed as per steps 1–8 above were magnified (i.e., numerically resampled) by factors of 2 each in x- and y-directions. A cubic spline interpolation was used to divide the pixels into subpixels, with the flux kept conserved. As discussed further in § 6.7, our results do not depend much on whether or not the magnification is done.

Figures 1, 2, and 3 show the final reduced images for the noncoronagraphic F160W, noncoronagraphic F190N, and coronagraphic F160W observations. The orientations of Figures 1 and 2 agree exactly, while they differ from that of Figure 3 by only 2°.026. All three images have essentially zero background. The F190N image shows a weak residual flat field and nonuniformities in the corners caused by amplifier glow. This effect is much less noticeable in the reduced F160W image. We believe that the F190N image is limited by the quality of the F190N flat field available to us. The F190N flat field, made from six 192 s long in-flight exposures to calibration lamps, has a count rate of 37.72 ADU s^{-1}, while the F160W flat, made from nine 24 s exposures, has a count rate of 1113 ADU s^{-1}. The rms deviation in the count rate per pixel is about 2% for each of the six frames combined to make the F190N flat, while it is about 0.02% for each of the nine frames combined to make the F160W flat. The lack of a better F190N flat is unfortunate. However, this should not be a serious problem for the quasar and DLA images, since they lie in the central part of the array. Figures 1 and 2 show the quasar point source along with the diffraction pattern. The coronagraphic image in Figure 3 shows the quasar light to be reduced

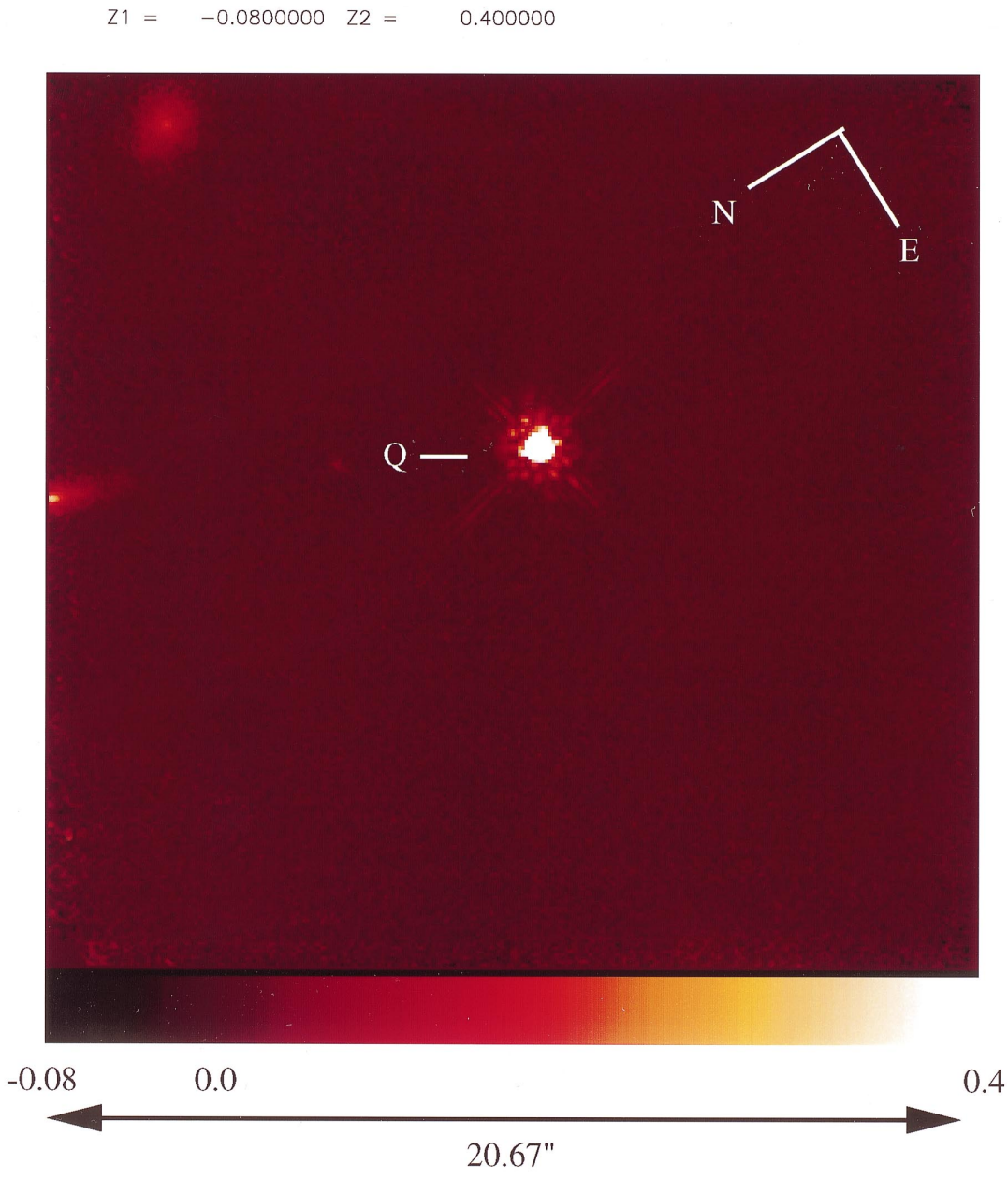

FIG. 1.—NICMOS camera 2 noncoronagraphic 1.6 μm broadband image of the field of LBQS 1210+1731. The color scheme is indicated with the bar on the bottom of the image. The flux scale in ADU s^{-1} is indicated on the color bar. Image y-axis is −121°.961 east of north.

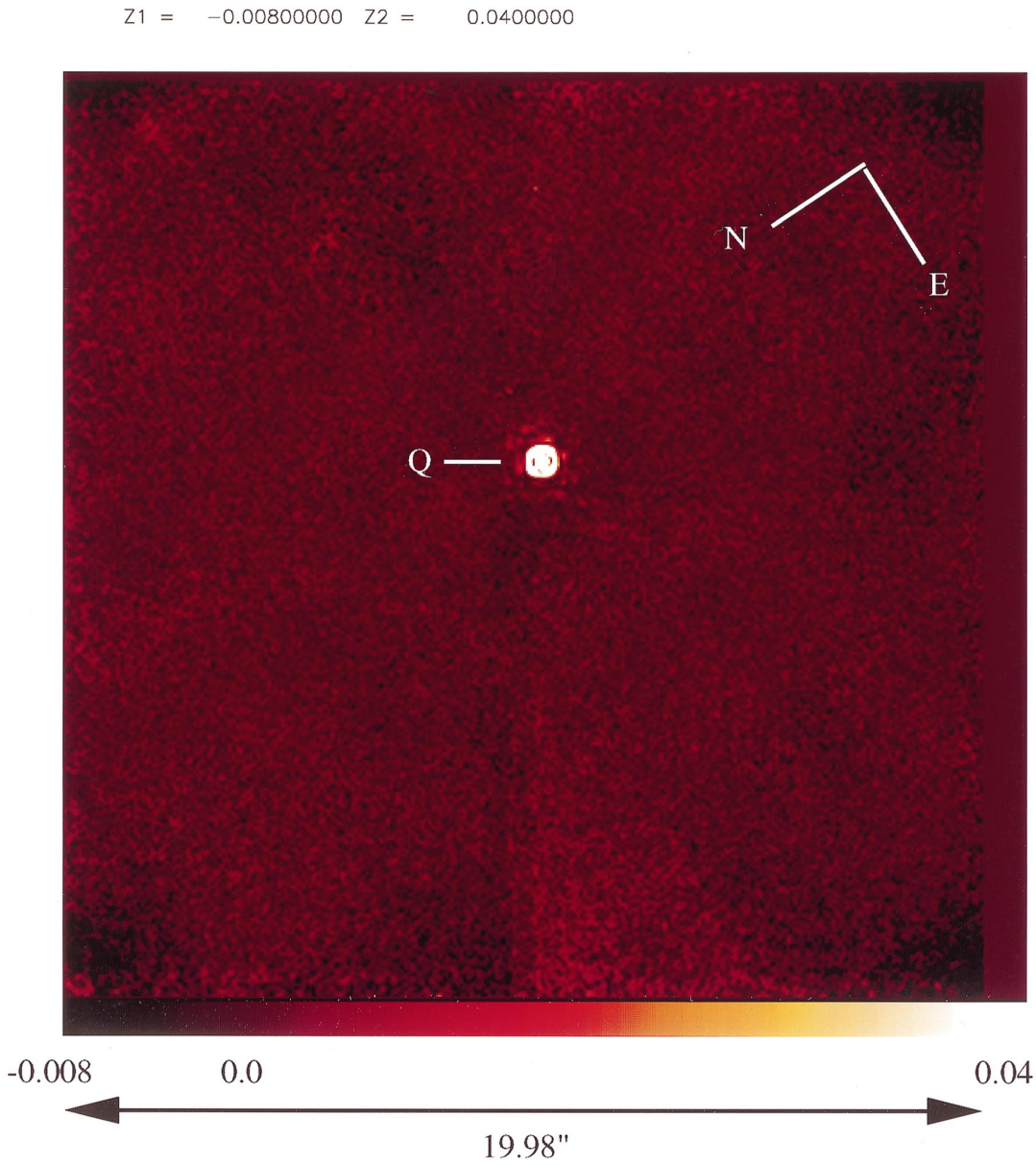

FIG. 2.—NICMOS camera 2 noncoronagraphic 1.9 μm narrowband image of the field of LBQS 1210+1731. Image y-axis is −121°961 east of north.

greatly, although not completely. To study whether there is any additional underlying faint emission from the DLA in any of these images, we need to subtract the respective PSFs.

4. SUBTRACTION OF THE QUASAR POINT SPREAD FUNCTION

4.1. *Selection of the PSF Star*

Reference point-spread functions for subtraction were obtained by using observations of stars in the same filter/aperture combinations as those employed for the quasar imaging. PSF star observations were not included in our own observations since we wanted to maximize the use of the available *HST* observing time for imaging of the quasar fields. We therefore used PSF star observations from other programs (in particular the stellar images from the photometric monitoring program carried out during Cycle 7 NICMOS calibration) for constructing the reference PSFs for subtraction. Such directly observed PSFs, when exposed to high signal-to-noise ratios (S/Ns), are expected to provide better match to the quasar data than the theoretical TINY TIM PSFs (since the observed PSFs incorporate any real optical effects not simulated in TINY TIM). We have also actually experimented with the use of calculated TINY TIM PSFs and find that they do indeed provide poorer match to the quasar than the observed stellar PSFs.

For the noncoronagraphic images, the PSF observations were chosen such that the telescope focus "breathing" (Bely 1993) values matched as closely as possible the values for the DLA observations. This is important because changes in the *HST* focus translate into corresponding changes in the fine structure of the PSF. To estimate the OTA focus positions for the epoch of the quasar and PSF star observations, we used the *HST* focus ephemerides provided by STScI (Hershey 1998; Hershey & Mitchell 1998). For the

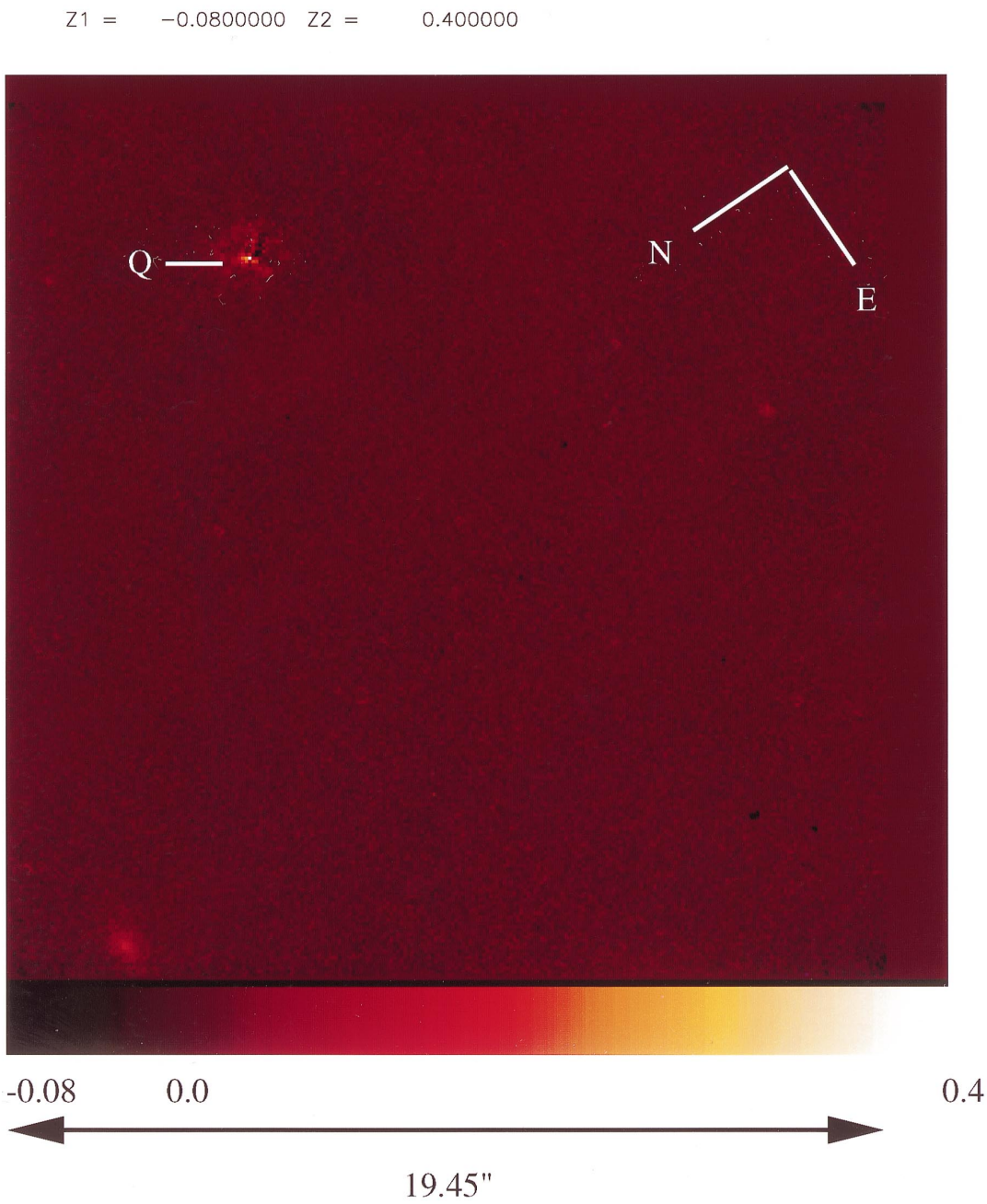

FIG. 3.—NICMOS camera 2 coronagraphic 1.6 μm broadband image of the field of LBQS 1210+1731. The quasar has been placed in the coronagraphic hole. Image y-axis is −123°.987 east of north.

noncoronagraphic F160W and F190N images, we used the PSF star P330E, observed on 1998 July 8 and 1998 May 29, respectively. We also studied the effect of PSF variations on our results by using PSF observations of P330E with a range of different breathing focus positions obtained on different dates and also by using observations of other PSF stars. (See §§ 6.2 and 6.3 for a detailed description.) The F160W noncoronagraphic image of P330E, made by combining four exposures of 3 s each, had a count rate of 108.10 ADU s^{-1} at the maximum of the first Airy ring. The corresponding quasar image, made by combining five exposures of 512 s each, had a count rate of 1.91 ADU s^{-1} at the maximum of the first Airy ring. For the F190N filter, the P330E image, made by combining three exposures of 64 s each, had 0.055 ADU s^{-1} at the maximum of the first Airy ring. The corresponding count rate was 0.0013 ADU s^{-1} for the F190N quasar image, made by combining 20 exposures of 704 s each.

For the coronagraphic observations, the choice of the PSF star was guided by the requirement that the position of the star in the coronagraphic hole be as close as possible to that of the quasar in our observations. This is critical, because even when the target-acquisition flight software succeeds in acquiring the target and putting it in the coronagraphic hole, there are usually some small residual differences between the actual position where the target is placed and the desired position of the target in the hole, i.e., the "low scatter point" of the coronagraph (see Schneider

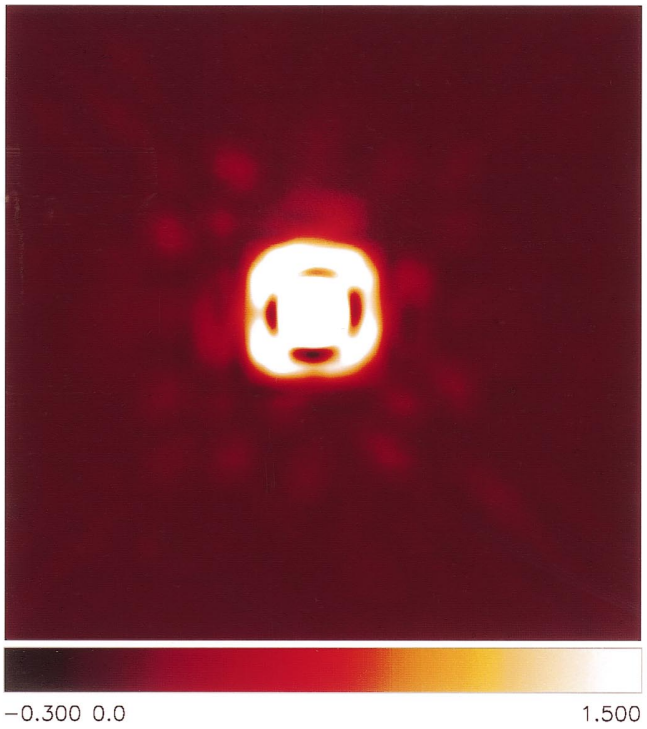

FIG. 4.—Zoomed-in 2.″74 × 2.″71 region of the NICMOS camera 2 noncoronagraphic 1.6 μm broadband image of the field of LBQS 1210+1731 (*top*) before PSF subtraction and (*bottom*) after PSF subtraction. The residual feature is labeled "O1" in the bottom panel.

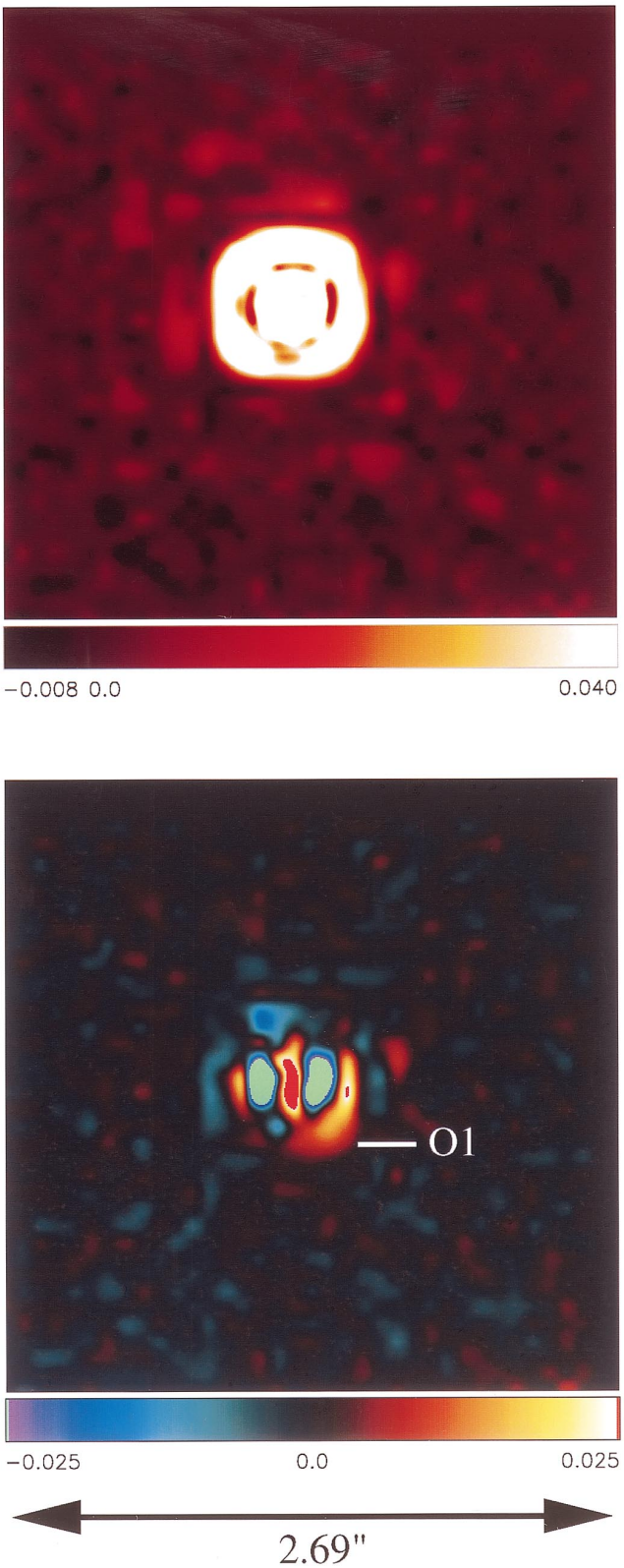

FIG. 5.—Zoomed-in 2.″69 × 2.″66 region of the NICMOS camera 2 noncoronagraphic 1.9 μm narrowband image of the field of LBQS 1210+1731 (*top*) before PSF subtraction and (*bottom*) after PSF subtraction. The residual feature is labeled "O1" in the bottom panel.

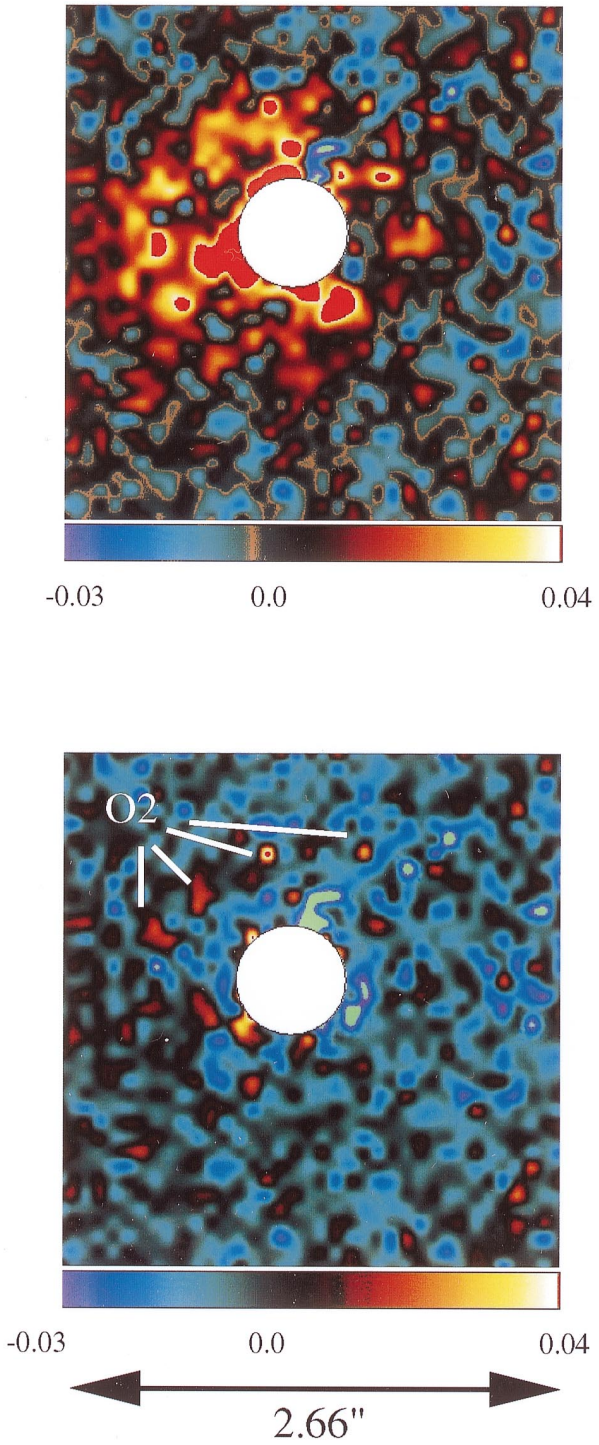

FIG. 6.—Zoomed-in 2.″66 × 2.″71 region of the NICMOS camera 2 coronagraphic 1.6 μm broadband image of the field of LBQS 1210+1731 (*top*) before PSF subtraction and (*bottom*) after PSF subtraction. The four residual features are labeled "O2" in the bottom panel.

1998 for details). The PSF wings and "glints" from the edge of the coronagraphic hole depend sensitively on the precise position of the point source within the hole. We therefore used the observations of star GL 83.1 for which we had coronagraphic observations (from another NICMOS GTO program), with the star placed at a position within 0.04 pixels of the position of the quasar LBQS 1210+1731 in our data. The observations of GL 83.1 were taken on 1998 August 1 at a breathing value close to that for our quasar coronagraphic observations.

For all the "primary" PSF star choices, the proximity of the observation dates with those of our quasar observations also ensures that the plate scale of the camera is the same for the PSF and the quasar observations.

4.2. *Subtraction of the PSF Star*

All of the observations of the PSF star P330E were obtained in four-point spiral dither patterns in steps of 4.″0 (≈52.6 pixels). The dithers for the PSF star were obtained by using actual spacecraft movements, while the dithers for LBQS 1210+1731 were obtained by moving the field offset mirror (FOM) internal to NICMOS. However, the use of the FOM should not cause any differences between the combined quasar PSF and the reference star PSF, since we registered all of the quasar exposures individually to a common reference before combining. The PSF star observations were analyzed in exactly the same manner as the quasar observations, following the procedure outlined in § 3. The same interpolation scheme was used for resampling of the PSF star and quasar images. The difference in the dithering steps for the quasar and the PSF star may give rise to difference in actual sampling of the quasar and PSF star images. However, as described in § 6.7, we have verified that the difference images are reproduced well when both the quasar and PSF star images are numerically resampled by a factor of 2. The final reduced PSF star images were subtracted from the corresponding quasar images after suitable scaling and registration, using the interactive data language (IDL) program IDP-3 (Lytle et al. 1999). The scale factors were chosen using the relative intensities of the PSF wings in the quasar image and the PSF star image. For the coronagraphic image, the relative intensities of the PSF glints near the edge of the hole were also used in determining the PSF scaling factor. All the parameters (i.e., relative x and y alignment of the PSF star image with respect to the quasar image and the intensity scaling factor for the PSF star image) were fine tuned iteratively to obtain the minimum variance in roughly 3″ × 3″ subregions (around the quasar) in the PSF-subtracted image. Radial plots of the quasar image, the aligned and scaled PSF image, and the difference of the two were also examined to check the alignment and scaling of the PSF. Figures 4 (*top*), 5 (*top*), and 6 (*top*) show zoomed ≈3″ × 3″ subregions around the quasar, from the noncoronagraphic F160W, noncoronagraphic F190N, and coronagraphic F160W images shown in Figures 1, 2, and 3, respectively. Figures 4 (*bottom*), 5 (*bottom*), and 6 (*bottom*) show the PSF-subtracted versions of Figures 4 (*top*), 5 (*top*), and 6 (*top*), respectively, using the closest matching PSFs available.

5. RESULTS

5.1. *Noncoronagraphic F160W Images*

Figure 4 (*bottom*) shows the F160W image after subtraction of the PSF image of star P330E obtained on 1998 July 8. The fidelity of the PSF subtraction is seen from the fact that the diffraction pattern disappears completely and most of the residual image contains a random mixture of positive and negative values. The radially symmetric residuals may be explained, for the most part, by a mismatch between the spectral energy distribution (SED) of the quasar and that of the PSF star (spectral type G2 V). These color terms lead to

small differences in the structure and size scale of the PSFs. These differences are nonnegligible under the $\approx 25\%$ bandpass of the F160W filter but are negligible under the 1% bandpass of the F190N filter. See § 6.3 for further discussion. The main asymmetric residual is the emission feature to the "lower right" of the center, about 3 pixels (0.″26) away from the center. (This feature is seen more clearly if the data are subsampled by a factor of 2, as discussed further in § 6.7 and Fig. 15.) There is no correspondingly strong and symmetrically located negative feature in the image, and the bright knot can not be made to disappear after reregistration of the PSF and quasar images or rescaling of the PSF image without causing large negative residuals elsewhere (see § 6.9 and Fig. 18). We cannot completely rule out that this "knot" is an artifact in the PSF. However, given the significant excess over a number of pixels, it is likely that it is a real feature. This feature (which we name object "O1") is about 0.″40 long. If this emission knot is associated with the damped Lyα absorber at $z = 1.892$, then it is $\approx 2.4\ h_{70}^{-1}$ kpc long for $q_0 = 0.5$, or 3.2 h_{70}^{-1} kpc long for $q_0 = 0.1$. In § 6, we examine in detail the question of whether or not O1 is real. In this section we discuss the properties of O1 assuming that it is real and is associated with the DLA absorber.

The faintness and diffuse nature of object O1 make its photometry rather difficult. We estimated the flux from this object in the PSF-subtracted image, using three different procedures, and then took an average of the three values.

Since accurate aperture photometry is difficult, we first estimated the flux by subtracting the PSF star from object O1, now multiplying the star by a factor large enough to make object O1 look indistinguishable from noise. This PSF multiplying factor can then be used directly to estimate the flux of object O1, since the PSF star P330E is a well-calibrated NICMOS photometric standard. From this method, we deduce that object O1 is 2.55×10^{-4} as bright as the PSF star P330E. This implies a flux of 3.22 ADU s^{-1} or 7.1 μJy in the F160W filter. To convert the count rate to flux, we used the NICMOS photometric calibration factor of 2.190×10^{-6} Jy/(ADU s^{-1}) for the F160W filter. This factor was derived using the solar-type photometric standard star P330E (which we also used for PSF subtraction).

As a rough check of the above flux value, we also did aperture photometry on a circular aperture 4 pixels in diameter centered on O1 using the IRAF task APPHOT. A constant background value was subtracted as the sky value. (This constant, estimated as the average of the mean values per pixel of about 20 10 × 10 subregions in different parts of the image, had a very low mean value and therefore made negligible change to the final flux values.) This yields 2.55 ADU s^{-1}, i.e., 5.6 μJy before correcting for aperture effects. For reference, the 1 σ noise level in the PSF-subtracted image is about 0.13 ADU s^{-1} pixel^{-1} (0.28 μJy pixel^{-1}) in a circular annulus 0.″2 wide centered at 0.″3 from the quasar center. The corresponding noise levels at 0.″5, 0.″7, 0.″9, and 1.″1 from the quasar center are 0.023, 0.014, 0.012, and 0.012 ADU s^{-1} pixel^{-1} (i.e., 0.051, 0.031, 0.027, and 0.026 μJy pixel^{-1}, respectively).

The 4 pixel diameter circular aperture covers most of the region of emission in O1 and avoids the residuals near the center of the quasar and very narrow features that we think arise from residual PSF differences. This region, however, does not include the pixels at the extreme ends of the "major axis" of O1, which is about 6 pixels long. We therefore also estimated the flux by doing a pixel-by-pixel addition over the region actually occupied by O1, which gives 2.63 ADU s^{-1}, i.e., 5.8 μJy. The flux values estimated by both the aperture photometry methods need to be corrected for the fact that a significant fraction of the energy of even a point source lies outside the radius of 2 pixels. Using aperture photometry on the standard star P330E, we estimate that the aperture correction factor between radii $r = 2$ and $r = 7.5$ pixels is 1.625. A further factor of 1.152 has been estimated for camera 2 filter F160W for the aperture correction from a 7.5 pixel radius aperture to the total flux, based on standard NICMOS photometric calibrations made with the standard star P330E. Thus, the total aperture correction factor is 1.872 for the second method. We note, however, that there is a roughly 10% uncertainty in the aperture correction factor. Schneider et al. have estimated the above correction factor to be 2.08. Taking an average, we adopt an aperture correction factor of 1.98 ± 0.1. Since the region used in the third method is approximately also 4 pixels in diameter (although slightly bigger near the ends of the "major axis" of O1), the aperture correction is (at least) 1.98 in this case. We therefore use this factor for the third method of flux estimation also, although it is hard to be sure of the exact aperture correction in this case. After the aperture corrections, we derive flux values of 11.0 μJy with the second method and 11.4 μJy with the third method.

On averaging the three flux values derived above, we estimate a flux of 9.8 ± 2.4 μJy for the flux from object O1. This corresponds to $m_{\rm F160W} = 20.11^{+0.30}_{-0.24}$ (taking 0 mag to correspond to 1083 Jy in the Johnson system). Here we have used equal weights for the three values while averaging, although we note that the value obtained by subtracting a point source is likely to be more accurate than the other two values. Note that the error estimate indicates the standard deviation among the three flux estimates obtained by the three methods and thus reflects the uncertainties in the size and shape of object O1. For comparison, the 1 σ uncertainty in the background near O1 is 0.051 μJy pixel^{-1}, or ≈ 0.2 μJy over the region of ≈ 12 pixels occupied by O1.

The observed F160W flux corresponds to a luminosity (at a mean rest-frame wavelength of 0.55 μm) of about $1.5 \times 10^{10}\ h_{70}^{-2}\ L_\odot$ for $q_0 = 0.5$ and about $2.8 \times 10^{10}\ h_{70}^{-2}\ L_\odot$ for $q_0 = 0.1$. Thus, object O1 is fainter than an L_* galaxy at $z = 1.89$ by 0.2–0.9 mag. If O1 is not the DLA, the DLA is even fainter. Our results here are consistent with those of Djorgovski (1997), who reported a possible counterpart to the $z = 4.10$ DLA toward DMS 2247−0209. That DLA candidate is located $\approx 3.''3$ from the quasar (i.e., 22 h_{70}^{-1} kpc for $q_0 = 0.1$), with an inferred continuum luminosity of $0.5L_*$.

5.2. *Noncoronagraphic F190N Images*

At a redshift of $z_{\rm DLA} = 1.892$, any Hα emission would be expected to lie at $\lambda_{\rm obs} = 1.898$ μm, which is very close to the center and mean λ of 1.900 μm for the filter F190N. Thus, the narrowband images in filter F190N are expected to reveal any redshifted Hα emission from the DLA. Figure 5 (*bottom*) shows the PSF-subtracted F190N image using the PSF image of the star P330E observed on 1998 May 29. The residual image shows an emission feature in roughly the same place ($\approx 0.''28$ away from the quasar center to the lower right) and with roughly the same size (0.″42 long) as the feature seen in the noncoronagraphic F160W image. This feature is more clearly evident if the images are sub-

sampled by a factor of 2 (as discussed in § 6.7 and Fig. 16). As in the F160W image, this feature also does not disappear after realigning or rescaling the PSF. This suggests that feature O1 may be a real object. If O1 is associated with the DLA absorber at $z = 1.892$, the absorber is $\approx 2.5\ h_{70}^{-1}$ kpc long for $q_0 = 0.5$, or $\approx 3.4\ h_{70}^{-1}$ kpc long for $q_0 = 0.1$.

As in the case of the broadband images, the photometry of O1 is rather difficult. We do it in three different ways and take an average. In an attempt to get a flux estimate free of the uncertain aperture correction factor, we first subtracted the standard star P330E from O1, scaling the star such that the feature O1 just disappears. This method gives a flux in O1 of 4.11×10^{-4} times that of P330E. This corresponds to a flux of 0.204 ADU s^{-1}, i.e., 9.1 μJy. Here we have used the NICMOS photometric calibration factor of 4.455×10^{-5} Jy/(ADU s^{-1}) for the F190N filter. Aperture photometry yields a flux of 0.114 ADU s^{-1} in a 4 pixel diameter circular aperture centered on the center of O1. A pixel-by-pixel addition over the region occupied by O1 gives a flux of 0.132 ADU s^{-1}. Based on the photometry of the standard star P330E, we estimate that the aperture correction factor between $r = 2$ and $r = 7.5$ is 1.691. The aperture correction factor between $r = 7.5$ and the total flux is expected to be 1.159 for the F190N filter. This implies a total aperture correction factor of 1.960 for the $r = 2$ values. However, a $\approx 10\%$ uncertainty exists in the aperture correction factor, similar to that discussed above for the F160W images. We therefore adopt an average aperture correction factor of 2.06. Applying this aperture correction, we get flux values of 0.234 ADU s^{-1} (10.4 μJy) and 0.272 ADU s^{-1} (12.2 μJy), respectively, for the second and third methods. Averaging the three flux values obtained by the three methods, we get 10.6 ± 1.5 μJy. The error bar of 1.5 μJy denotes only the standard deviation among the three values and thus reflects the uncertainties arising from the lack of knowledge about the size and shape of O1. For comparison, the 1 σ noise levels in the F190N image (after PSF subtraction) at $r =$ 0.″5, 0.″7, 0.″9, and 1.″1 from the quasar are 0.0027, 0.0019, 0.0018, and 0.0016 ADU s^{-1} $pixel^{-1}$, i.e., 0.119, 0.084, 0.081, and 0.073 μJy $pixel^{-1}$, respectively. Thus, the 1 σ sky noise uncertainty in the total summed flux over the ≈ 12 pixel region occupied by O1 is ≈ 0.4 μJy (using the noise estimates just outside O1 at $r = 0.''5$).

The expected F190N continuum must be subtracted from the observed flux in order to determine if a statistically significant redshifted Hα excess exists. We estimate the continuum under the F190N filter by scaling the F160W image using the relative photometric calibration of the two filters. We find that, in fact, this expected continuum flux agrees almost completely with the observed F190N flux. After subtraction of the expected F190N continuum image (scaled from the F160W image) from the observed F190N image, we find a very marginal excess of 0.0074 ADU s^{-1}. With the aperture correction, this corresponds to 0.68 μJy. The 1 σ noise level in the F190N–F160W image is 0.0026 ADU s^{-1} $pixel^{-1}$ just outside the location of O1. This noise level corresponds to a 1 σ uncertainty of 0.4 μJy in the total flux summed over the region occupied by O1. The slight excess at the location of O1 in the F190N–F160W image is thus not statistically significant. We therefore conclude that the contribution to the F190N flux from redshifted Hα emission is negligible. It is not likely that we could have missed the Hα emission from O1. The Hα emission from the DLA could lie outside the F190N bandpass only if the DLA galaxy is lower in velocity by more than 980 km s^{-1} or higher in velocity by more than 1770 km s^{-1} from the absorption redshift. Such offsets are higher than the observed internal velocity dispersion in any typical single galaxy.

Integrating over the FWHM of the F190N filter, assuming no dust extinction, and using the prescription of Kennicutt (1983) for conversion of Hα luminosity to SFR, the nominal marginal excess of 0.68 μJy in the F190N–F160W image corresponds to an SFR of $1.1\ h_{70}^{-2}\ M_\odot\ yr^{-1}$ for $q_0 = 0.5$, or $2.0\ h_{70}^{-2}\ M_\odot\ yr^{-1}$ for $q_0 = 0.1$. To derive a better estimate of the uncertainty in the Hα flux, we experimented with subtractions of the PSF-subtracted F190N and F160W images. In a 4 pixel region (roughly the size of our resolution element), an Hα emission strength of about 0.016 ADU s^{-1} (0.71 μJy) would yield S/N = 3. With an aperture correction factor of 3.41, this corresponds to a total 3 σ flux limit of 0.054 ADU s^{-1} or 2.4 μJy. This translates into a 3 σ upper limit on the SFR of $4.0\ h_{70}^{-2}\ M_\odot$ yr^{-1} for $q_0 = 0.5$ or $7.4\ h_{70}^{-2}\ M_\odot\ yr^{-1}$ for $q_0 = 0.1$. (We consider the possibility of dust extinction in § 7.3 below.)

5.3. *Coronagraphic F160W Images*

An F160W coronagraphic image of the quasar is shown in Figure 6 (*top*), in which the coronagraphic hole is masked out. Almost all the flux seen in this reduced coronagraphic image is due to residual scattered light from the quasar and glints from the edge of the hole. After subtraction of a reference PSF image using observations of the star GL 83.1, these artifacts disappear almost entirely (Fig. 6 [*bottom*]). The bright emission feature about 0.″25 to the lower right of the quasar center, seen in Figures 4 (*bottom*) and 5 (*bottom*), is just inside the coronagraphic hole and is therefore not seen in Figure 6 (*bottom*). However, the coronagraph is very effective in reducing the quasar light outside of the coronagraphic hole and can therefore be used to look at other objects in the field.

A weak feature (which we name object "O2") remains after PSF subtraction (to the top left of the hole, about 0.″7 away from the quasar center). This feature is dominated by four knots of continuum emission. No artifacts resembling this feature have been seen in the coronagraphic images of PSF stars from other NICMOS GTO programs. By contrast, the knots seen to the lower left are known artifacts in the coronagraphic PSF. O2 is detected in the same place if the data for each of the two orbits are analyzed separately, which suggests that it may be real. It is not likely to be a trail of a cosmic-ray event, since it is present in the images over a period of 2 orbits (much longer than typical timescales for the decay of cosmic-ray persistence in the NICMOS detectors). The knots in feature O2 are much weaker than the peak in feature O1 but are about 2–3 times the rms noise in the background. O2 has a total linear size of about 9–10 pixels, i.e., about 0.″7–0.″8. The 1 σ noise levels per pixel in the PSF-subtracted image at 0.″3, 0.″5, 0.″7, 0.″9, and 1.″1 from the quasar center are 0.032 ADU s^{-1}, 0.012 ADU s^{-1}, 0.011 ADU s^{-1}, 0.0088 ADU s^{-1}, and 0.0094 ADU s^{-1}, i.e., 0.069, 0.027, 0.024, 0.019, and 0.021 μJy $pixel^{-1}$, respectively. Compared to the noncoronagraphic F160W image, these noise levels indicate factors of 4.06, 1.88, 1.30, 1.41, and 1.26 improvements, respectively, in the 1 σ sensitivities at 0.″3, 0.″5, 0.″7, 0.″9, and 1.″1 from the quasar center. These factors are much smaller than those typically reported for NICMOS coronagraphic performance,

because the low signal from our faint quasar makes our observations read noise dominated.

The results of coronagraphic imaging (e.g., appearance of object O2) are not expected to be very sensitive to the data reduction procedures. No dithering was used between the coronagraphic exposures to ensure that the quasar always remained in the coronagraphic hole. Therefore, the individual coronagraphic exposures were not registered before they were combined. The quasar was acquired with onboard target acquisition and placed in the coronagraphic hole at the beginning of the first orbit. The quasar was placed in the same position in the second orbit. Guide star acquisition was done at the beginning of each of the two orbits using the same guide stars. Therefore, we believe that there are no significant offsets between the quasar's positions in the hole in the various coronagraphic exposures. Indeed, as mentioned above, the coronagraphic images obtained in each orbit separately show the object O2, which appears similar in both the orbits. The fact that features in the coronagraphic PSF other than object O2 disappear after the PSF subtraction also suggests that object O2 is not the result of misregistration of the individual exposures. We therefore believe that object O2 is likely to be real.

This feature O2 is detected marginally in the noncoronagraphic F160W image (Fig. 4 [*bottom*]) because of the higher scattered light from the quasar in that image. We note that, while of lower sensitivity, the faint compact emission features to the top left of the quasar in this image are at positions similar to those of the O2 knots in the coronagraphic image. Object O2 is not seen in the narrowband image in Figure 5 (*bottom*). However, considering that it is much fainter than object O1, it is not entirely surprising that any emission from O2 is not detected in the narrowband images (which are about 10 times less sensitive, at the separation of O2 from the quasar). Considering this, and its faintness and larger angular distance from the quasar compared to O1, it is not completely clear whether the feature O2 has any connection with the DLA, but it may be associated with the DLA or its companions. It is also possible that objects O1 and O2 are associated with the host galaxy of the quasar rather than the DLA. We discuss this possibility further in § 7.4. If O2 is indeed associated with the DLA at $z = 1.892$, then it has a size of 4–5 h_{70}^{-1} kpc for $q_0 = 0.5$.

6. IS OBJECT O1 REAL?

In view of the low S/N of object O1 and its small angular separation from the quasar in our noncoronagraphic F160W and F190N images, we carried out a number of tests on the images to investigate whether O1 is real or merely an artifact of the data-reduction or PSF-subtraction procedures. Here we describe these tests, listing the potential sources of error that we investigated in each case, and the corresponding results.

6.1. *Is Minimum Variance the Right Criterion in PSF Subtraction?*

We have registered and normalized the PSF star by varying the position and multiplicative scaling factor of the PSF star so as to minimize the variance in the region of interest near the quasar. This seems to be the most objective way of judging the goodness of fit of the PSF subtraction. To determine whether any bias could be caused by the use of the minimum-variance criterion, we also verified that the results from this method are closely consistent with K. McLeod's method of forcing the intensity at the first Airy minimum to zero (see McLeod, Rieke, & Storrie-Lombardi 1999). The PSF star position given by the two methods for the optimum PSF subtractions in each case agree to within 0.002 pixels. The PSF normalization factors from the two methods agree to within about 2%. In either case, our broad conclusions about the nature of the residuals after PSF subtraction (including feature O1) are the same for both the methods. Therefore, we believe that our strategy of minimizing the variance is sound.

6.2. *Telescope Breathing Effects?*

To examine how sensitive the detection of the main emission knot O1 is to the fine structure of the PSF subtracted, we created a suite of difference images using a variety of reference PSFs for the noncoronagraphic broadband and narrowband images. We particularly sought to investigate the effects of *HST* breathing focus changes on our results. The changes in *HST* focus consist of two components. First, there is a long-term slow change caused by shrinkage in the Optical Telescope Assembly (OTA) of *HST* due to moisture desorption, which is periodically corrected by secondary mirror moves. In addition, short-term focus variations on the time scale of the *HST* orbit, arising from thermally driven displacements of the OTA secondary, can be even larger in magnitude than desorption correction compensations.

Figure 7 shows the effect of using various observations of the PSF star P330E on the noncoronagraphic F160W images. Figure 7 (*top left*) is the same as Figure 4 (*bottom*), while Figures 7 (*top right*), 7 (*bottom left*), and 7 (*bottom right*) show the results obtained by subtracting images of P330E taken on different dates and with different breathing values. The breathing values denote the position of the *HST* secondary mirror in units of μm with respect to a common reference, i.e., with respect to the best focus of WFPC2 planetary camera (see Hershey & Mitchell 1998). All four panels of Figure 7 show the feature O1 in roughly the same place with other variations being much smaller in amplitude than O1. Figure 8 shows the difference of the PSFs used in making Figure 7. Figures 8 (*top left*), 8 (*top right*), and 8 (*bottom*) show, respectively, PSF for Figure 7 (*top left*) − PSF for Figure 7 (*top right*), PSF for Figure 7 (*top left*) − PSF for Figure 7 (*bottom left*), and PSF for Figure 7 (*top left*) − PSF for Figure 7 (*bottom right*). The differences among the residuals in the different panels of Figure 8 arise partly from breathing variations. However, we note that the different dates for the reference PSF observations imply the use of different guide stars, and hence the PSF star would have landed on different pixels in these different images. Therefore, the intrapixel response function, in addition to focus changes, could also account for some of the differences between the different PSF images.[3] In any case, the symmetric nature of the residuals in Figure 8 and the absence of the knot O1 in these images suggests that the latter feature is present in the quasar images, and not an artifact in any individual PSF image.

Figure 9 illustrates the effect of telescope breathing focus variations on the F190N images, with three different obser-

[3] We further note that the breathing models of Hershey & Mitchell (1998) have some uncertainty. This could give rise to some residuals in our difference images arising from differential inaccuracies in the breathing values for the quasar and the PSF star images predicted by the models.

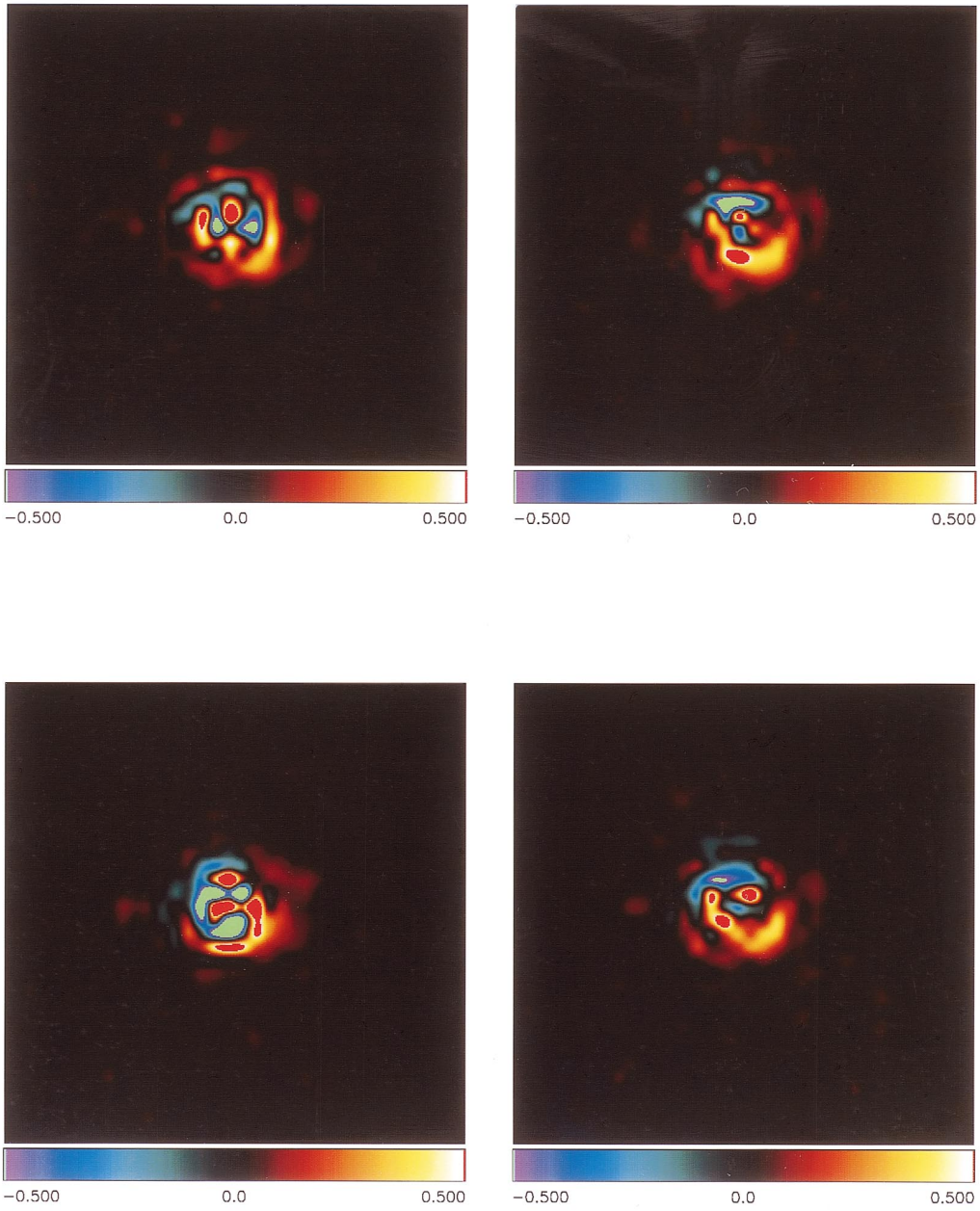

FIG. 7.—Effect of *HST* "breathing" focus variations on the PSF-subtracted F160W noncoronagraphic image. Zoomed-in 2.″74 × 2.″71 region of the NICMOS camera 2 noncoronagraphic 1.6 μm broadband image of the field of LBQS 1210+1731, on using images from four different observations of the PSF star P330E. The PSF star observation dates and breathing values are (*top left*) (1998 July 8; 1.0), (*top right*) (1998 August 9; 1.2), (*bottom left*) (1998 September 7; 0.7), and (*bottom right*) (1998 March 7; −1.7). The quasar observations were obtained on 1998 July 22 at breathing value of 2.2.

vations of PSF star P330E. Figure 9 (*top left*) is the same as Figure 5 (*bottom*). The corresponding PSF star differences are shown in Figure 10. Figures 10 (*left*) and 10 (*right*) show, respectively, PSF for Figure 9 (*top left*) − PSF for Figure 9 (*top right*), and PSF for Figure 9 (*top left*) − PSF for Figure 9 (*bottom*). The feature O1 is detected in the same place in all the panels of Figure 9, and most of it is not seen in the PSF star differences (Fig. 10).

6.3. *Using Different PSF Stars: Color Mismatch between Quasar and PSF Star?*

Color terms in the PSFs are potentially important sources of error in the difference images. For our primary PSF subtractions we have used the solar analogue P330E ($m_{F110W} - m_{F160W} = 0.44$, $m_{F160W} - m_{F222M} = 0.08$) as described in the previous section. However, we also experimented with a red PSF star BRI 0021 ($m_{F110W} - m_{F160W} = 1.17$, $m_{F160W} - m_{F222M} = 0.80$). Figure 11 shows the effect of using four different PSF stars (P330E, BRI 0021, Q1718PSF, and GSC 4) in the top left, top right, bottom left, and bottom right panels, respectively. Note that the breathing values for the four observations are quite different, which could explain the differences in the appearance of O1. In any case, all the images show an excess residual at the location of O1, while such excesses are not seen in the differences of the PSFs themselves (shown in Fig. 12). Thus, object O1 is probably not an artifact caused by color mismatch between the quasar and the PSF star.

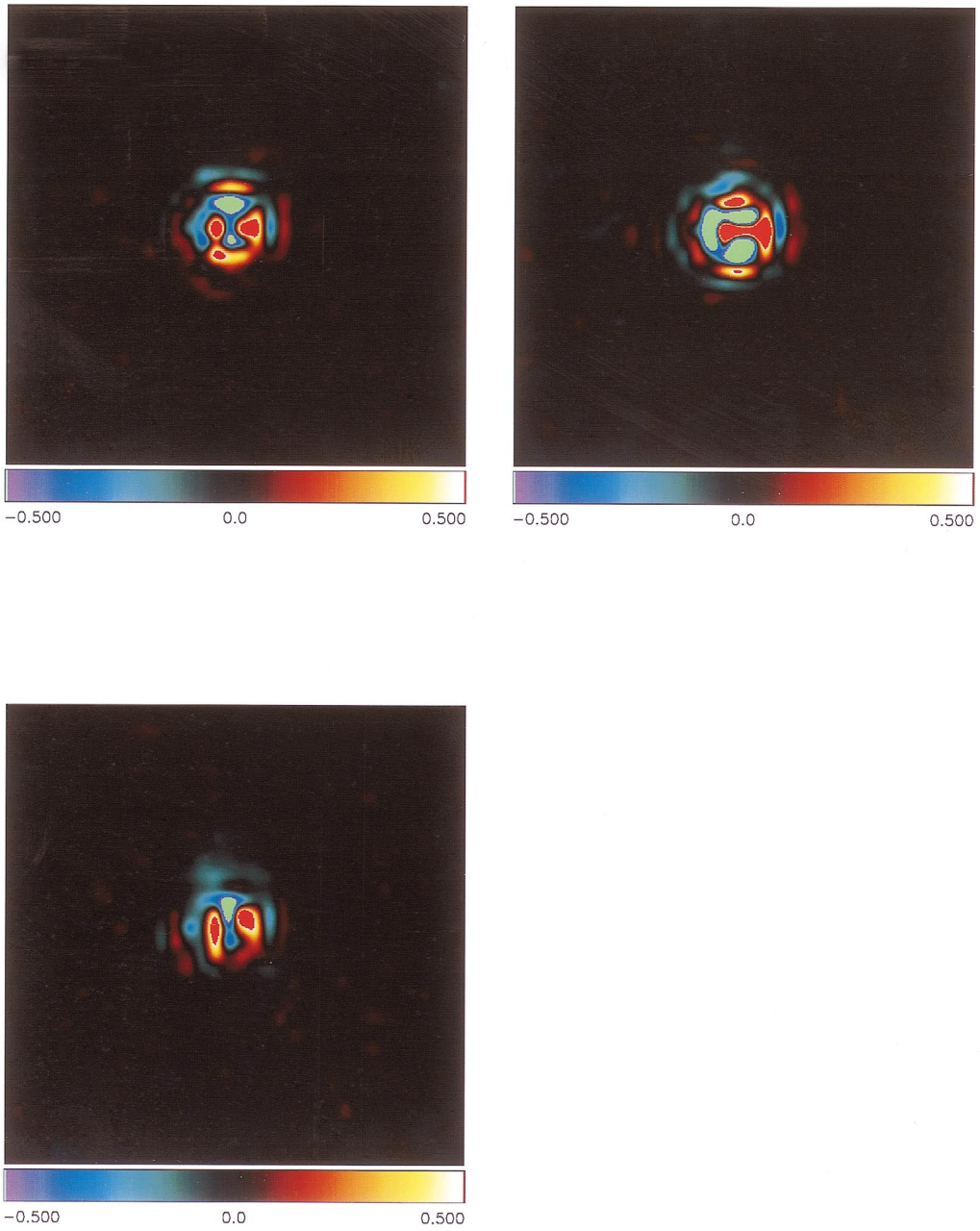

FIG. 8.—Differences of PSFs used in Fig. 7. (*top left*) PSF for Fig. 7 (*top left*) − PSF for Fig. 7 (*top right*), (*top right*) PSF for Fig. 7 (*top left*) − PSF for Fig. 7 (*bottom left*), (*bottom*) PSF for Fig. 7 (*top left*) − PSF for Fig. 7 (*bottom right*).

6.4. *Calibration Defects for Column 127 Influencing the Centroids?*

Two of our five dither positions for the noncoronagraphic F160W images had the quasar image near column 127 (in camera 2 detector coordinates). This column is well known to be "photometrically challenged." A "bad stripe" in this column results if the dark frame used for the calibration is not a perfect match to the dark current in the actual observations. We corrected for the "bad stripe" in this column by including it in the bad-pixel mask used while IMCOMBINEing the five dither positions. However, potentially this column may influence the centroids of the images at the two dither positions and hence the centroid of the IMCOMBINEd image. To explore this possibility, we looked at each of the three remaining dither positions not affected by column 127. Figure 13 shows central regions of the PSF-subtracted images for these three individual dither positions in top left, top right, and bottom left panels. The bottom right panel shows the result of PSF subtraction for the image obtained by combining only these three dither positions. For obtaining the minimum-variance solutions for these PSF subtractions, we have excluded the PSF cores while determining the variance. The first dither position as well as the combined image (*bottom right panel*) show an asymmetric excess emission near the position of object O1. This suggests that the feature O1 is not caused by errors arising from column 127, since none of the dither positions considered in Figure 13 include this column.

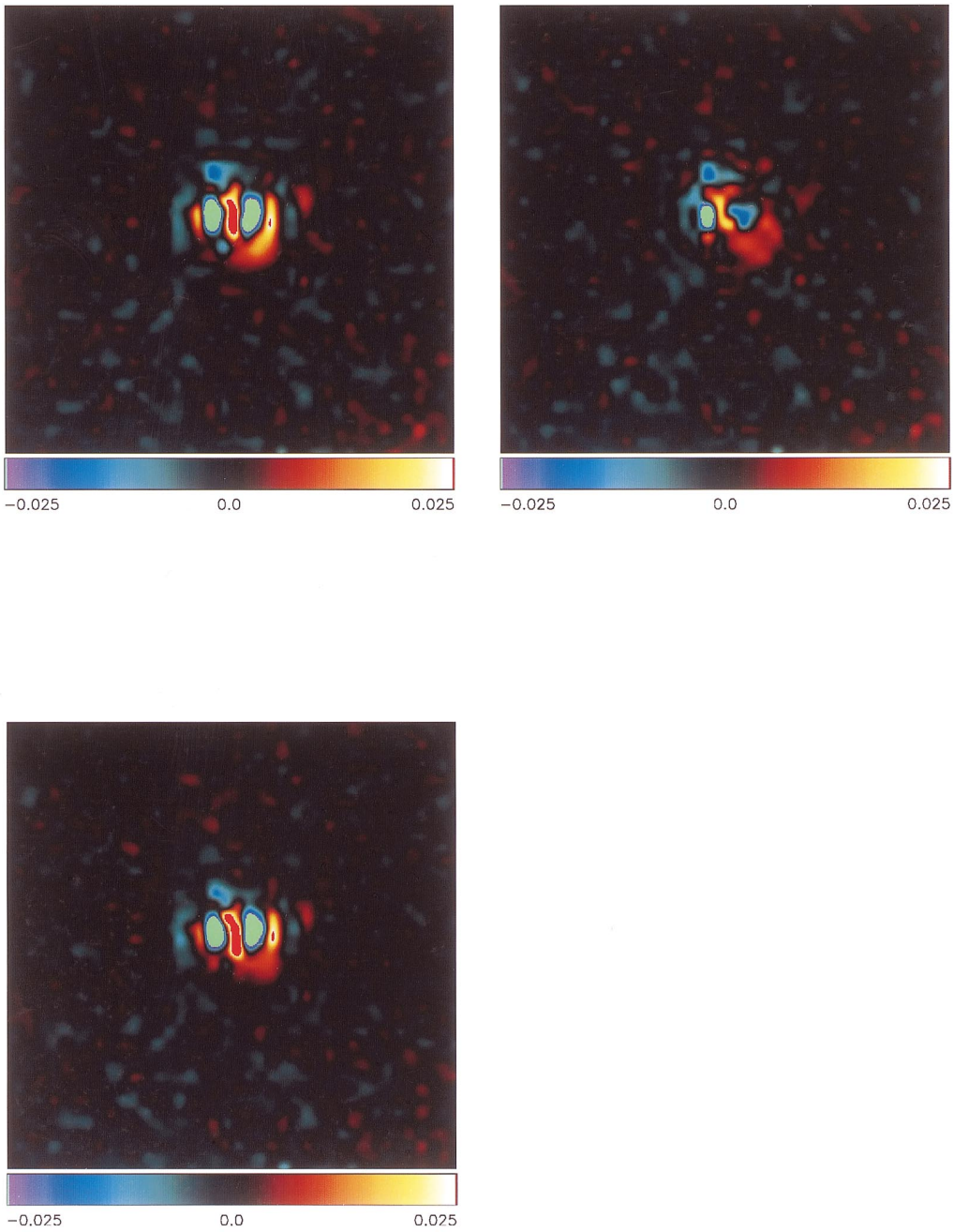

FIG. 9.—Effect of *HST* breathing focus variations on the PSF-subtracted F190N noncoronagraphic image. Zoomed-in 3.″04 × 3.″01 region of the NICMOS camera 2 noncoronagraphic 1.9 μm narrowband image of the field of LBQS 1210+1731, on using images from 3 different observations of the PSF star P330E. The PSF star observation dates and breathing values are (*top left*) (1998 May 29; 1.5), (*top right*) (1998 March 7; 1.3), and (*bottom*) (1998 July 8; 0.7). The quasar observations were obtained on 1998 July 22 at mean breathing value of 2.3.

6.5. *Persistence Effects from the Quasar Image at Previous Dither Positions?*

The experiments with PSF subtraction on the individual dithers described in test (6.4) above also help to show that image persistence effects are not important in causing feature O1. This is because even the very first dither position (which should not suffer from quasar persistence effects) shows the presence of an asymmetric feature at the location of O1 (*top left panel* of Fig. 13). Also, the quasar LBQS 1210+1731 is faint, so it is not likely to cause persistence effect. The fact that O1 has roughly equal intensity in all dither positions and does not go away even in the final dither position implies that O1 is also not a left over persistence image from a bright object or cosmic ray detected before the start of our observations.

6.6. *Difference between "Camera 1–2 Focus" versus "Camera 2 Focus"?*

Our quasar images were obtained with the NICMOS internal focusing mechanism optimized for parallel camera 1 and 2 operations, whereas all of our reference PSFs were taken at the camera 2 exclusive focus. A very slight deviation from confocality in the two cameras results in a wavefront error of 0.049 μm mm^{-1} of focal dispersion. The focus

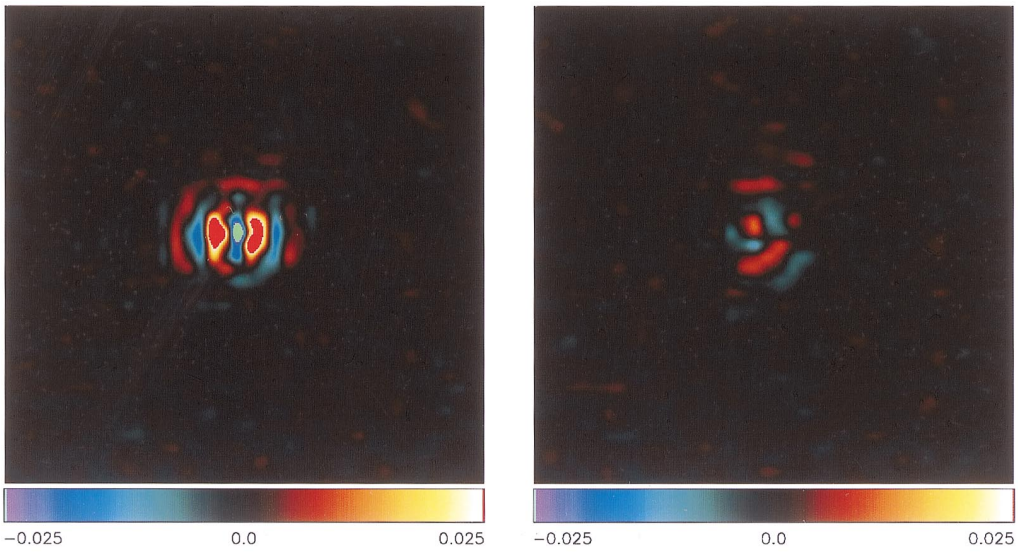

FIG. 10.—Differences of PSFs used in Fig. 9. (*left*) PSF for Fig. 9 (*top left*) − PSF for Fig. 9 (*top right*), (*right*) PSF for Fig. 9 (*top left*) − PSF for Fig. 9 (*bottom*).

error in camera 2 at the critically sampled λ (1.75 μm) is $\lambda/33$ with the focus at the common position. While small, this focus error can affect the fine structure of the PSF to a very small degree, as higher order aberrations also change (with an aggregate power of about one-half the focus error).

To investigate whether this effect can give rise to feature O1, we took two approaches. In the first approach, we used images of a star actually observed at the compromise focus "camera 1–2." There were no systematic PSF star measurements made at this focus position during the NICMOS calibration program. However, we found a star in one of our images of the galaxy cluster CL 0939+47 taken for another NICMOS GTO program. Figure 14 (*top left*) shows the PSF subtraction results obtained for our quasar image using this observed PSF at the compromise focus. The fact that some of the features in O1 are still seen while some disappear suggests that some of the O1 features (e.g., the blob to the right of the core) could be real.

In the second approach, we constructed simulated NICMOS camera 2 PSFs using the TINY TIM program (version 4.4; Krist & Hook 1997). We constructed simulated PSFs for the two pupil alignment mirror (PAM) positions corresponding to the two foci at the time of our quasar observations on 1998 July 22 and the P330E observations on 1998 July 8. These two simulated TINY TIM PSFs differ only in this focus position and both used the same values of rms jitter (0.″007), same x and y pixel positions for placement of PSF star center, same pixel size, etc. After making these two simulated PSFs, we corrected them for the slight relative difference in the actual x and y plate scales (interpolated in time for the dates of the observations for LBQS 1210+1731 and the observations for P330E). This slight repixelization corrects for the fact that TINY TIM creates images with equal x and y pixel scales, whereas the actual x and y pixel scales differ by 0.9%. The difference of the two simulated TINY TIM PSFs corrected for the unequal x and y pixel scales is shown in Figure 14 (*top right*). The difference does show some residuals along the diagonal directions. However, these are symmetric in shape on both sides of the center and are accompanied by much larger residuals in the core of the image. Figure 14 (*bottom left*) shows, on the same stretch as Figure 14 (*top left*), the difference of the two simulated TINY TIM PSFs after normalizing each to match the quasar. The residuals in Figure 14 (*bottom left*) are much weaker than object O1. A simple relative translation between the images for the two foci cannot give rise to a feature as significant as O1 without causing a much larger residual in the core. We therefore conclude that while the difference in the PAM positions for the quasar and the PSF star could cause some of the residuals in our PSF subtractions, they cannot be the major source of these residuals.

To pursue this analysis further, we took the ratio of the two simulated TINY TIM PSFs after correction for plate scales[4] and multiplied this ratio by the actual observed P330E PSF to make our "best-guess" PSF. The resultant PSF has the advantages of combining the correct focus (PAM) position (because of the TINY TIM simulation), the best estimate of breathing (because of use of the actual observation of P330E, which matches closely in breathing with the LBQS 1210+1731 data), and any other actual optical effects that TINY TIM does not simulate adequately. In the bottom right panel of Figure 14, we show the resultant image obtained after subtracting this "best-guess" synthetic P330E PSF from the LBQS 1210+1731 data. Once again, excess emission is seen at the position of O1. This suggests that O1 is not caused by artifacts of relative focus difference ("camera 1–2" focus vs. "camera 2" focus) between the quasar and the PSF star.

6.7. *Errors in Imcombining or Interpolating the Dithers?*

We used NICRED 1.8 to interpolate the registered dithers onto a grid of single camera 2 pixels, or onto a grid of half-integer camera 2 pixels. This magnification (repixelization) or lack thereof made little difference in the

[4] Here by the ratio of the simulated TINY TIM PSFs, we mean the ratio of the PSF with the PAM position for LBQS 1210+1731 to the PSF with the PAM position for the star P330E, the same two PSFs whose difference is shown Figures 14 (*top right*) and 14 (*bottom left*).

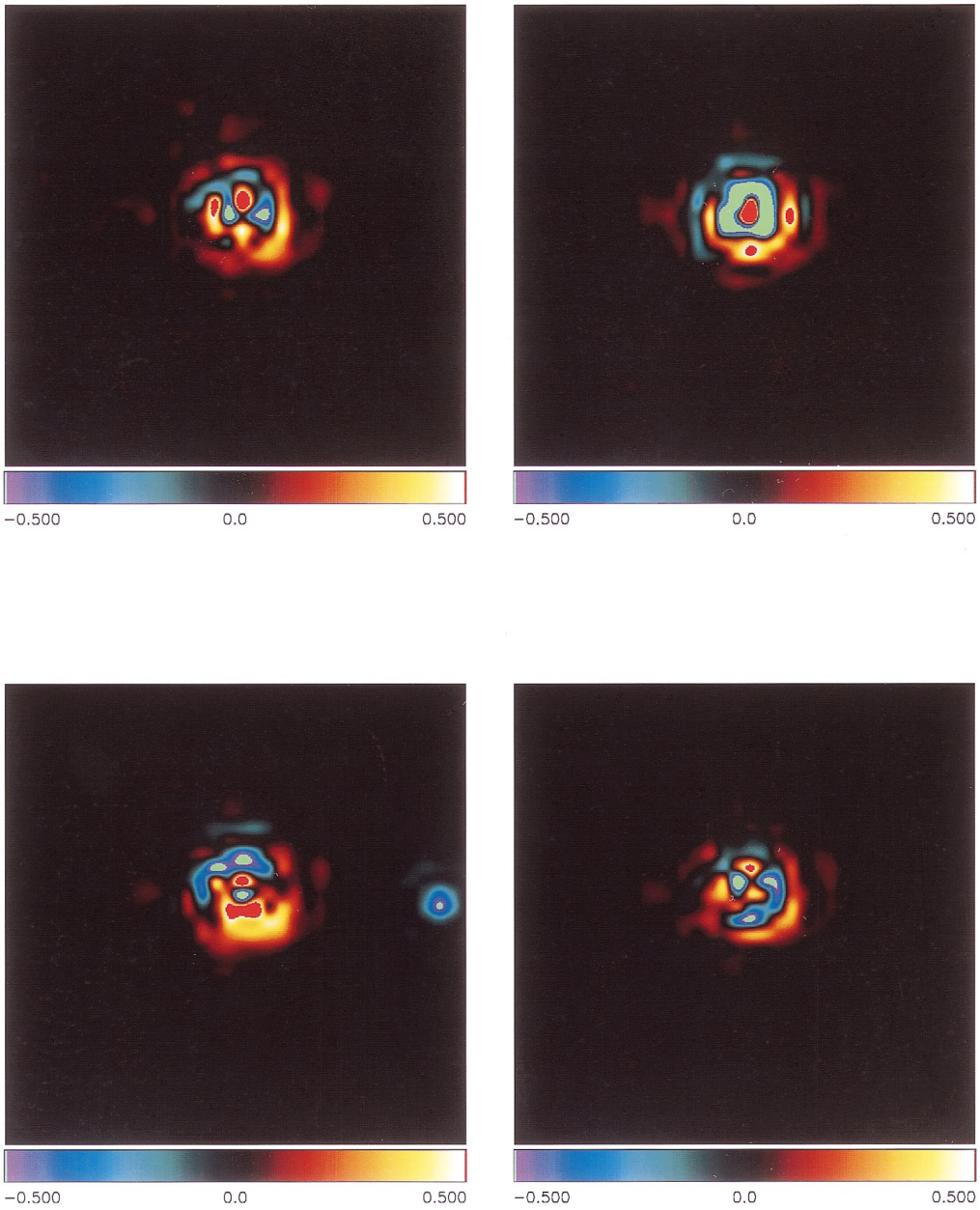

FIG. 11.—Effect of using different PSF stars on the PSF-subtracted F160W noncoronagraphic image. Zoomed-in 2.″74 × 2.″71 region of the NICMOS camera 2 noncoronagraphic 1.6 μm broadband image of the field of LBQS 1210+1731, on using PSF stars P330E, BRI 0021, Q1718PSF, and GSC 4. The PSF star observation dates and average breathing values are (*top left*) (1998 July 8; 1.0), (*top right*) (1997 December 20; −1.2), (*bottom left*) (1998 July 21; 1.8), and (*bottom right*) (1997 November 11; −3.2). The quasar observations were obtained on 1998 July 22 at mean breathing value of 2.3. The differences between the different panels may be largely because of breathing differences. (The match with the quasar breathing value is poor for the right panels, while it is best for the bottom left panel.) The negative feature near the right edge of (*bottom left*) is because of a second star near the main PSF star used for subtraction.

result. This is clear from Figure 15, which shows the F160W images made on using grids of single camera 2 pixels (Fig. 15 [*top left*]) and half-integer camera 2 pixels (Fig. 15 [*top right*]). Figures 15 (*bottom left*) and 15 (*bottom right*) show the same figures with pixel replication instead of cubic convolution interpolation in the IDP3 display. The similarity between the left and right panels is reassuring and results from camera 2 being nearly critically sampled at 1.6 μm. The same was also found to be true for the F190N images. Figure 16 shows the F190N images made on using grids of single camera 2 pixels and half-integer camera 2 pixels (Figs. 16 [*top left*] and 16 [*top right*] shown with cubic convolution and Figs. 16 [*bottom left*] and 16 [*bottom right*] shown with pixel replication). Both Figures 15 and 16 suggest that object O1 is likely to be real and does not arise from interpolation errors.

6.8. *Effects of Asymmetries or Saturation in the Core?*

Based on our experience with other NICMOS GTO data, the core of the PSF often shows paired positive and negative residuals after PSF subtraction. In case the core of the quasar and PSF star images have some asymmetries that might mimic an O1-like feature after PSF subtraction, we have also done the PSF subtraction without including

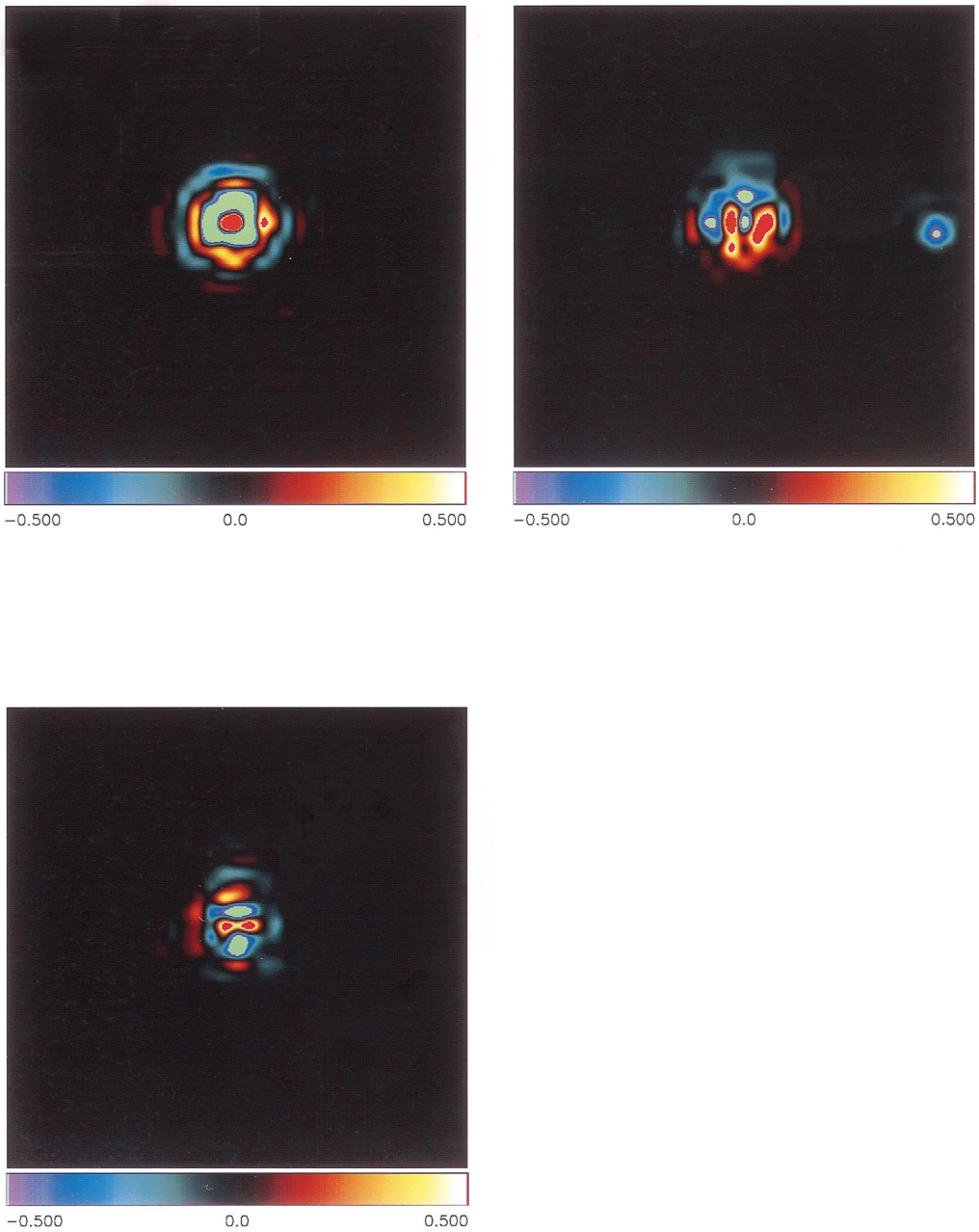

FIG. 12.—Differences of PSFs used in Fig. 11. (*top left*) PSF for Fig. 11 (*top left*) − PSF for Fig. 11 (*top right*), (*top right*) PSF for Fig. 11 (*top left*) − PSF for Fig. 11 (*bottom left*), and (*bottom*) PSF for Fig. 11 (*top left*) − PSF for Fig. 11 (*bottom right*). The negative feature near the right edge of (*top right*) is because of a second star near the main PSF star used for subtraction in Fig. 11 (*bottom left*).

the core for the variance calculation. The right panel in Figure 17 shows the noncoronagraphic F160W image obtained after minimizing the variance in the PSF subtraction without including the core of the image for variance calculation. The region thus excluded, shown with a circular mask, covers the region up to the first Airy minimum. The left panel in Figure 17 shows the noncoronagraphic F160W image obtained when the core is included (same as the image shown in Fig. 4 [*bottom*], except that the central core is masked in the display only for easy comparison with the right panel of Fig. 17). The similarity between the two panels of Figure 17 (presence of a feature at the position of O1) suggests that asymmetries in the core are not the source of O1.

This same experiment also shows that saturation in the core of the quasar image cannot be a major problem (since the results obtained by including or excluding the core agree very closely). The individual 512 s exposures at each of the five dither positions in the F160W image of our quasar have peaks of about 15,000 ADU or 83,000 e^- in the quasar central pixel. Thus, we do expect that they should not be saturated, given the 98% linearity saturation limit of 173,000 e^- for camera 2.

6.9. *Errors in Alignment of PSF Star with Respect to the Quasar?*

Figure 18 shows the effects of shifting the PSF star by 0.1 pixel in various directions relative to the quasar on the

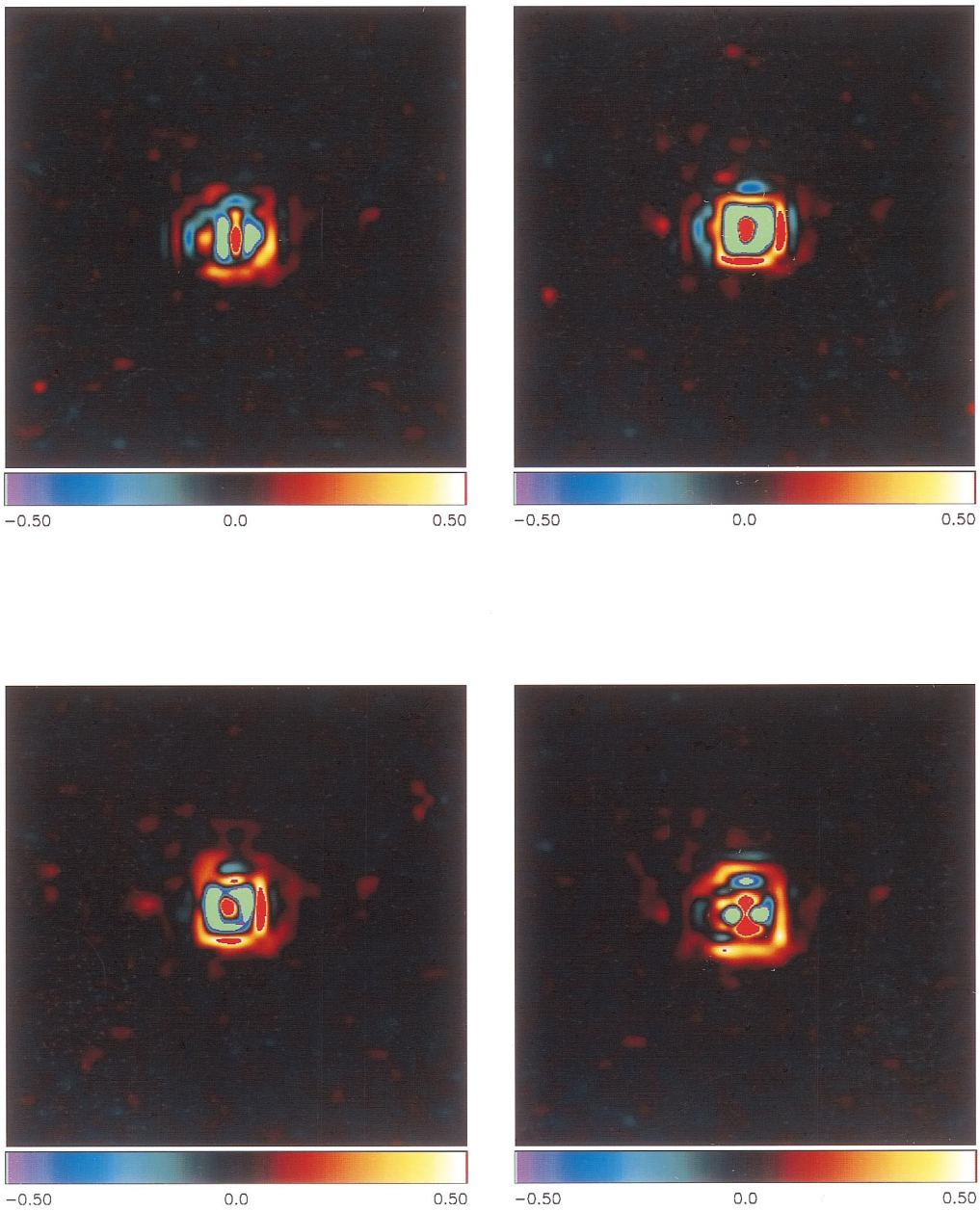

FIG. 13.—Effect of using different individual dither positions on the PSF-subtracted F160W noncoronagraphic image. Zoomed-in 3″.12 × 3″.09 region of the field of LBQS 1210+1731, on using (*top left*) position 1, (*top right*) position 4, and (*bottom left*) position 5 in the spiral-dither pattern. *Bottom right*: Result of combining the three positions.

difference F160W images. Figure 18*e* is the optimum minimum-variance solution (same as Fig. 4 [*bottom*]). Figures 18*b*, 18*h*, 18*d*, and 18*f* show the PSF subtractions obtained after shifting the PSF star by 0.1 pixel in the top, bottom, left, and right directions, respectively, with respect to the quasar. Figures 18*a*, 18*c*, 18*g*, and 18*i* show the corresponding results on shifting the PSF star by 0.1 pixel in the upper left, upper right, lower left, and lower right directions, respectively, with respect to the quasar. The large residuals in the core caused by even the slight shifts illustrate that the PSF star is very well aligned with respect to the quasar in the optimum PSF subtraction (Fig. 18*e*). We have shown shifts of 0.1 pixel in Figure 18 to make the changes easier to view. However, judging by the minimum in the variance, we believe that our relative alignment of the quasar and PSF star images is good to at least 0.01 pixel. Thus, errors in alignment of the PSF star with respect to the quasar should be insignificant.

6.10. *Errors in Stacking the Individual Dither Positions?*

The different dither positions are registered in NICRED 1.8 using cross-correlation. To check the accuracy of the image registration, we compared the centroids of the images at the various dither positions after registration. The 1 σ variation among the centroid values of the different dither images was found to be about 0.04–0.06 pixels, for both the quasar and the PSF star. The centroid values for any individual dither position calculated from different methods

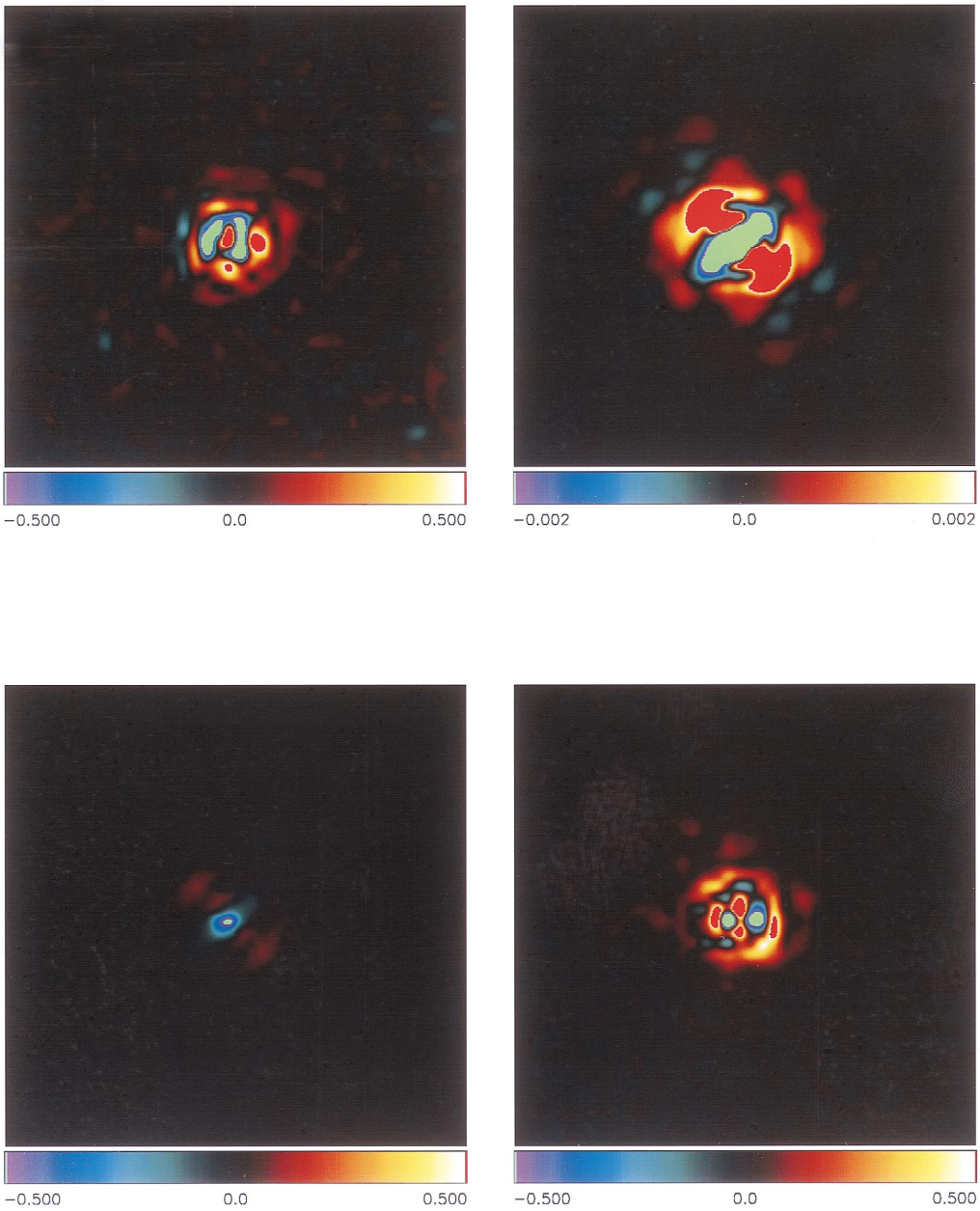

FIG. 14.—Effect of different focus positions on the PSF-subtracted F160W noncoronagraphic image. Zoomed-in 3.″12 × 3.″09 region of the NICMOS camera 2 noncoronagraphic 1.6 μm broadband image of the field of LBQS 1210+1731. (*top left*) PSF subtraction obtained on using PSF star image from the field of galaxy cluster CL 0939+47, which has the same camera 1–2 focus as our quasar data. (*top right*) Difference of two simulated TINY TIM PSFs corresponding to the camera 2 focus and camera 1–2 focus. (*bottom left*) On the same intensity stretch as (*top right*), the difference of the two simulated TINY TIM PSFs after normalizing each to match the quasar. (*bottom right*) Quasar image after subtracting a synthetic PSF made by multiplying the 1998 July 8 image of P330E by the ratio of the TINY TIM models for the two foci. See the text for details.

(tasks IMEXAM, CENTER, and STARFIND in IRAF) were also found to agree within about 0.06 pixels. Thus, there is a small uncertainty in the centroid values, but it does not seem large enough to cause a feature such as O1. The fact that the individual dither positions show some excess at the position of O1 (Fig. 13) also suggests that O1 is not a spurious feature resulting from stacking errors.

6.11. *Comparison with Other Data*

1. *Comparison of PSF stars with each other.*—PSF stars seem to subtract very well from each other, with the same caveat about color and breathing. There is no hint of a 1% residual at the position corresponding to the feature O1 (see Fig. 12).

2. *Same reduction on other quasar data.*—We reduced the data for quasar Q1718+4807 at $z = 1.084$ (a quasar without a DLA absorber) from another NICMOS GTO program, using the same reduction and PSF subtraction procedures as we have used for LBQS 1210+1731. We do not see the object O1 there.

We have also reduced the data for the other quasars with DLAs from our sample, which will be described in separate papers (Kulkarni et al. 2000, in preparation). Comparing the results for LBQS 1210+1731 with the results for those

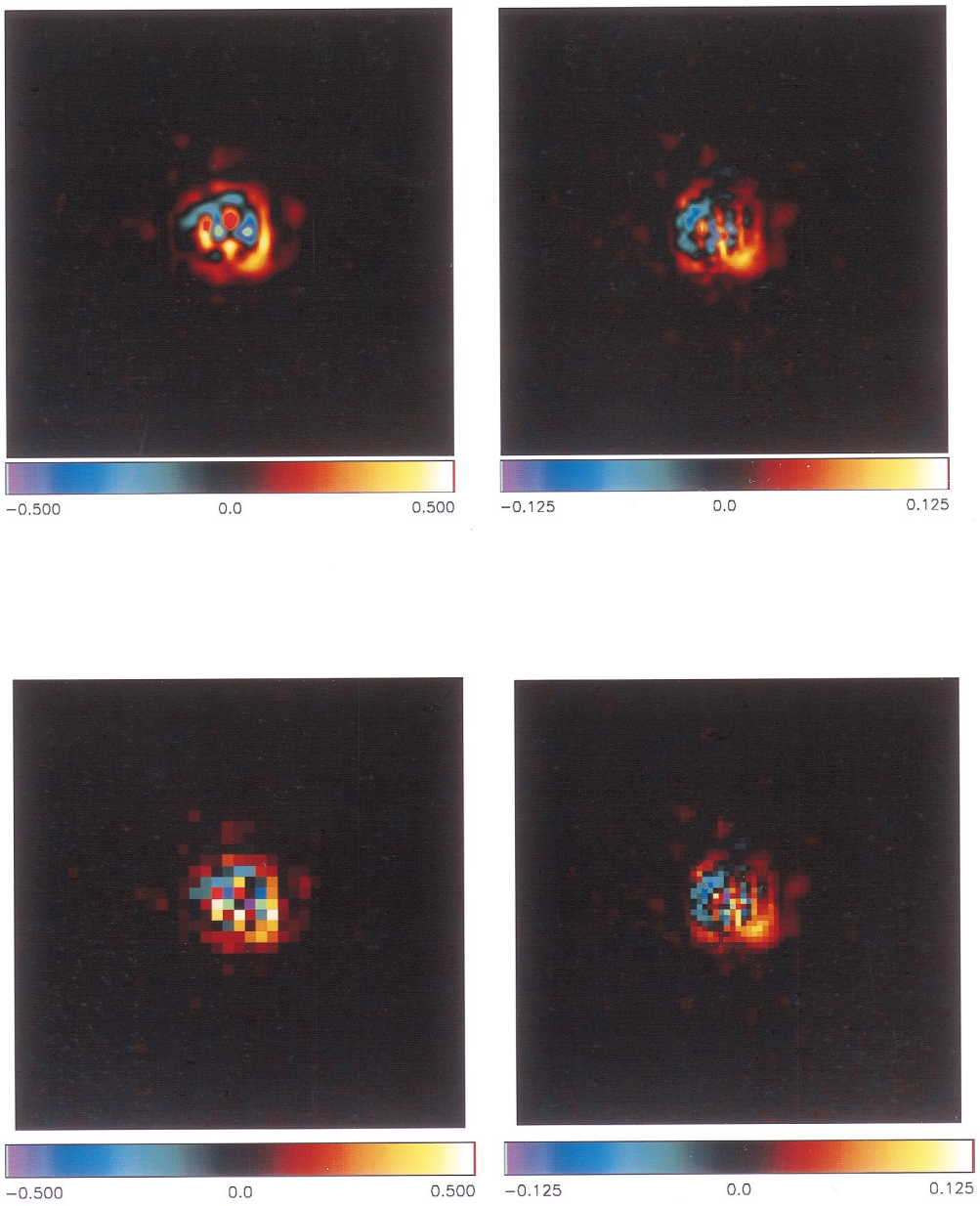

FIG. 15.—Effect of different magnification schemes in data reduction and different interpolation schemes in image display on the PSF-subtracted F160W noncoronagraphic image. Zoomed-in 3″.12 × 3″.09 region of the F160W image for (*top left*) no magnification in image analysis, bicubic interpolation in image display, (*top right*) magnification by a factor of 2 and bicubic interpolation in image display, (*bottom left*) no magnification and pixel replication in image display, and (*bottom right*) magnification by a factor of 2 and pixel replication in image display. Note the similarities between the magnified and unmagnified images, resulting from camera 2 being almost critically sampled at 1.6 μm.

quasars, we find that some of the residuals in the PSF subtractions appear similar, while some of the features are different. This suggests that part of the emission at the position of O1 is likely to be real, although part of it could be some artifact that we have not yet understood despite the large number of data analysis experiments described above.

6.12. *Summary of Results from Various Data Analysis Tests*

Overall, we conclude that the best-fitting PSF and several others with reasonably close breathing values suggest a possible detection of an object (object O1) located at about 0″.25 from the quasar center in both the F160W and F190N images. The appearance and properties of this object are more sensitive to the important step of PSF subtraction than to other data reduction steps such as flat fielding. However, our extensive tests suggest that this object is not an artifact of color or focus mismatch or spatial misalignment between the quasar and PSF star images. It is also not caused by image persistence or saturation or by the procedures used for interpolation or stacking of the individual images. We therefore believe that object O1 is likely to be real.

The most relevant broadband and narrowband summary images showing object O1 are the zoomed, magnified, PSF-subtracted images in Figures 15 (*top right*) and 16 (*top right*). The small angular separation of O1 from the quasar suggests that it is likely to be associated with the DLA absorber. The corresponding impact parameter is 1.5 h_{70}^{-1}

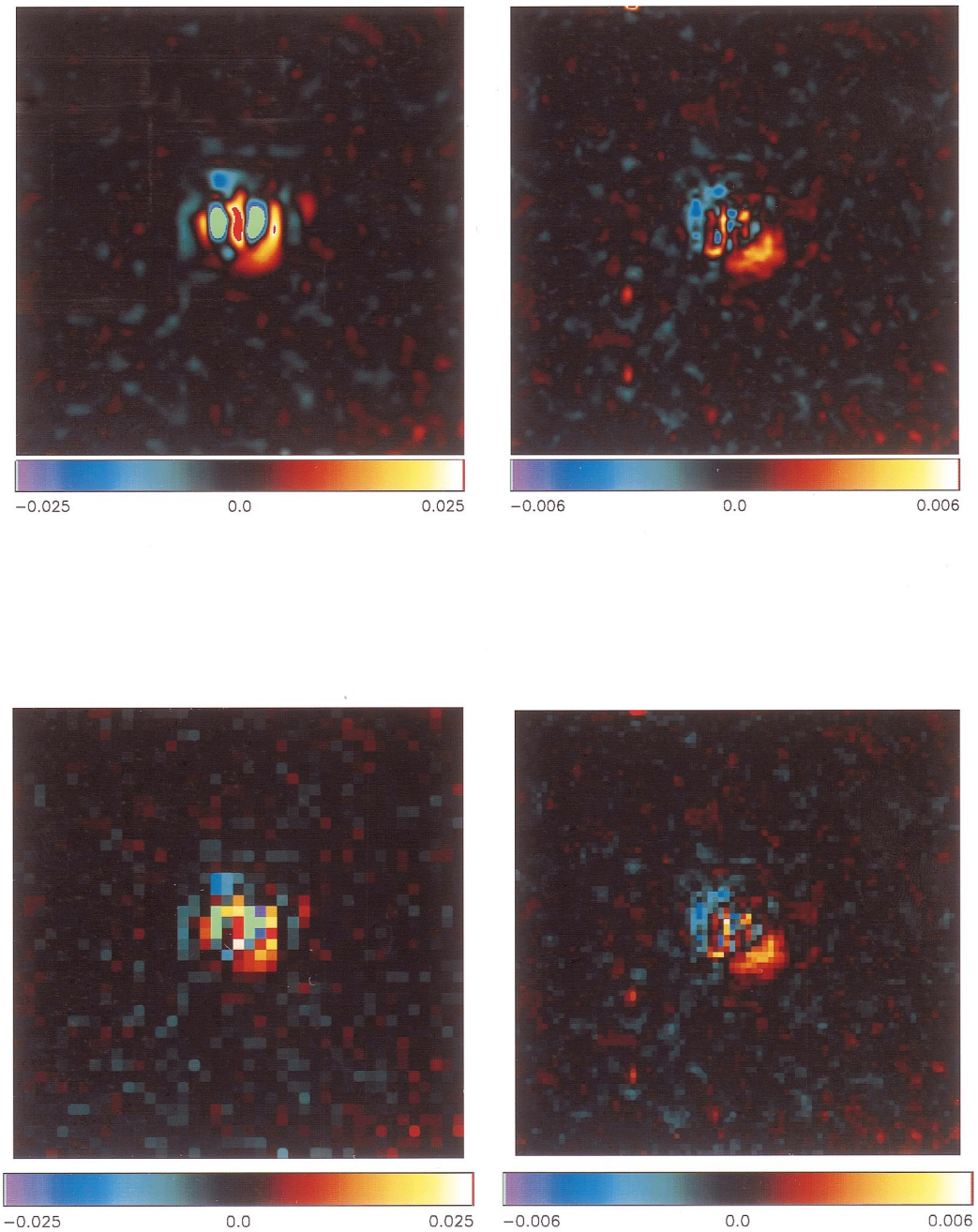

FIG. 16.—Effect of different magnification schemes in data reduction and different interpolation schemes in image display on the PSF-subtracted F190N noncoronagraphic image. Zoomed-in 3.″12 × 3.″09 region of the F190N image for (*top left*) no magnification in image analysis, bicubic interpolation in image display, (*top right*) magnification by a factor of 2 and bicubic interpolation in image display, (*bottom left*) no magnification and pixel replication in image display, and (*bottom right*) magnification by a factor of 2 and pixel replication in image display.

kpc for $q_0 = 0.5$ or 2.0 h_{70}^{-1} kpc for $q_0 = 0.1$. We have thus probed regions far closer to the quasar sight line than most previous studies of high-redshift intervening DLAs. Object O1 marks the closest detected high-redshift DLA candidate yet to any quasar sight line. Object O1 is 0.″4 long. If O1 is the DLA at $z = 1.89$, this translates into 2.4 h_{70}^{-1} kpc for $q_0 = 0.5$ or 3.2 h_{70}^{-1} kpc for $q_0 = 0.1$. It has a luminosity (at a mean rest-frame wavelength of 0.55 μm) of about 1.5×10^{10} h_{70}^{-2} $L_\odot$ for $q_0 = 0.5$ and about 2.8×10^{10} h_{70}^{-2} $L_\odot$ for $q_0 = 0.1$. Obejct O1 is thus fainter than an L_* galaxy at $z = 1.89$ by 0.2–0.9 mag. The comparison of the broadband and narrowband fluxes implies a nominal statistically insignificant SFR of 1.1 h_{70}^{-2} $M_\odot$ yr^{-1}, with a 3 σ upper limit of 4.0 h_{70}^{-2} $M_\odot$ yr^{-1}, for $q_0 = 0.5$.

Another, fainter object O2, which consists of four knots of continuum emission, is also seen in our images. (See Fig. 6 [*bottom*].) This object, at angular separation of 0.″65 from the quasar (well outside the first Airy ring of the quasar PSF) is also not a known artifact of the PSF. It is thus also likely to be real and may be a companion to the DLA. The spatial extent of O2 is 4–5 h_{70}^{-1} kpc, and its projected impact parameter is 3.8 h_{70}^{-1} kpc. Object O2, like object O1, is also closer to the quasar sight line than most other high-redshift DLA candidates detected before.

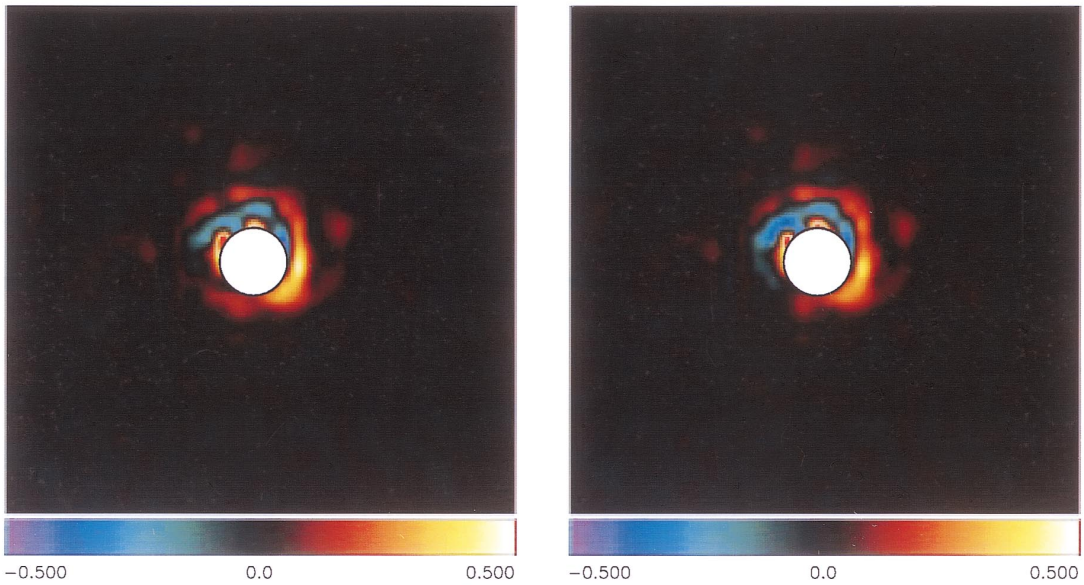

FIG. 17.—Effect of including or excluding the image core on the PSF-subtracted F160W noncoronagraphic image. Zoomed-in 2.″74 × 2.″71 region of the F160W image of the field of LBQS 1210+1731 obtained (*left*) including the region indicated by the circular mask and (*right*) excluding the region indicated by the circular mask. Note the similarity between the two panels.

We note, however, that because of the faintness and proximity of O1 to the quasar, we cannot completely rule out the possibility that this feature could partly be some as yet unknown artifact of the PSF (that is not simulated by TINY TIM either). If any such errors are the actual cause of O1, then the DLA absorber and the quasar host galaxy are even fainter than O1. In that case, we can use our images to put very sensitive upper limits on the size and brightness of both the DLA absorber and the quasar host. We discuss the implications of our observations in the following section.

7. DISCUSSION

The most important result from our observations is that there are no large bright galaxies close to the quasar in the field of the DLA absorber toward LBQS 1210+1731. Feature O1 is the most likely candidate for any object associated with the DLA. In §§ 7.1, 7.2, and 7.3, we assume that object O1 is associated with the DLA to derive constraints on various properties of DLAs. However, we also consider alternative possibilities in § 7.4, mainly the possibility that O1 may be associated with the host galaxy of the quasar.

7.1. *Constraints on Sizes and Morphology of DLAs*

Our observations show no evidence for a big, well-formed galaxy as expected in some scenarios for the DLAs (e.g., the protospiral model suggested by Wolfe et al. 1986; Prochaska & Wolfe 1997, 1998; Jedamzik & Prochaska 1998). Feature O1 has an estimated size of 2–3 h_{70}^{-1} kpc, while feature O2, if real, consists of small knots spread over about 4–5 h_{70}^{-1} kpc. Thus, these data suggest that the absorber is compact and clumpy, as expected in the hierarchical picture of galaxy formation. However, it is hard to be completely certain of the morphology, partly because of the sensitivity of the detailed image structure to the various factors discussed in § 6. Furthermore, it is possible that O1 and O2 are the brightest regions within a bigger galaxy, the rest of which we cannot see. Thus, we cannot completely rule out the large disk scenario, although the compact sizes and low SFRs suggest that the hierarchical picture may be favored. Analysis of the other DLAs from our sample and further deeper observations will help to more definitively distinguish between the large disk vs. hierarchical models.

7.2. *Constraints on Environment of DLA Absorbers*

Apart from features O1 and O2 very close to the quasar, our images show two prominent galaxies in the noncoronagraphic F160W image (one in the upper left corner or west of the quasar and the other at the middle of the left edge of the image or roughly north of the quasar—see Fig. 1). There is also a third very weak feature to the left (roughly north) of the quasar, a little less than one-half of the way along the line joining the quasar and the galaxy at the middle left edge. The galaxy west of the quasar is just barely apparent in the noncoronagraphic F190N image, while the other two objects are not seen in the noncoronagraphic F190N image. The two prominent galaxies in the noncoronagraphic F160W image are off the field of the coronagraphic image, while the prominent galaxy seen at the bottom edge (northeast) of the coronagraphic F160W image is off the field of the noncoronagraphic images. It is possible that the faint feature to the left (north) of the quasar is spurious. However, on running maximum-entropy and Lucy deconvolutions of the images, all the three objects (including the faint feature) in the F160W image were found to remain significant. These objects are likely to be galaxies in the same group as the DLA, although we do not have redshift information on them. In any case, they have fairly large impact parameters (4.″52, 11.″00, and 10.″96 for the faint feature, the galaxy to the west of the quasar, and the galaxy to the north of the quasar, respectively). At the redshift of the DLA absorber, these impact parameters would correspond to 26.8, 65.1, and 64.9 h_{70}^{-1} kpc, respectively, for $q_0 = 0.5$. For $q_0 = 0.1$, the corresponding values are 36.6, 89.0,

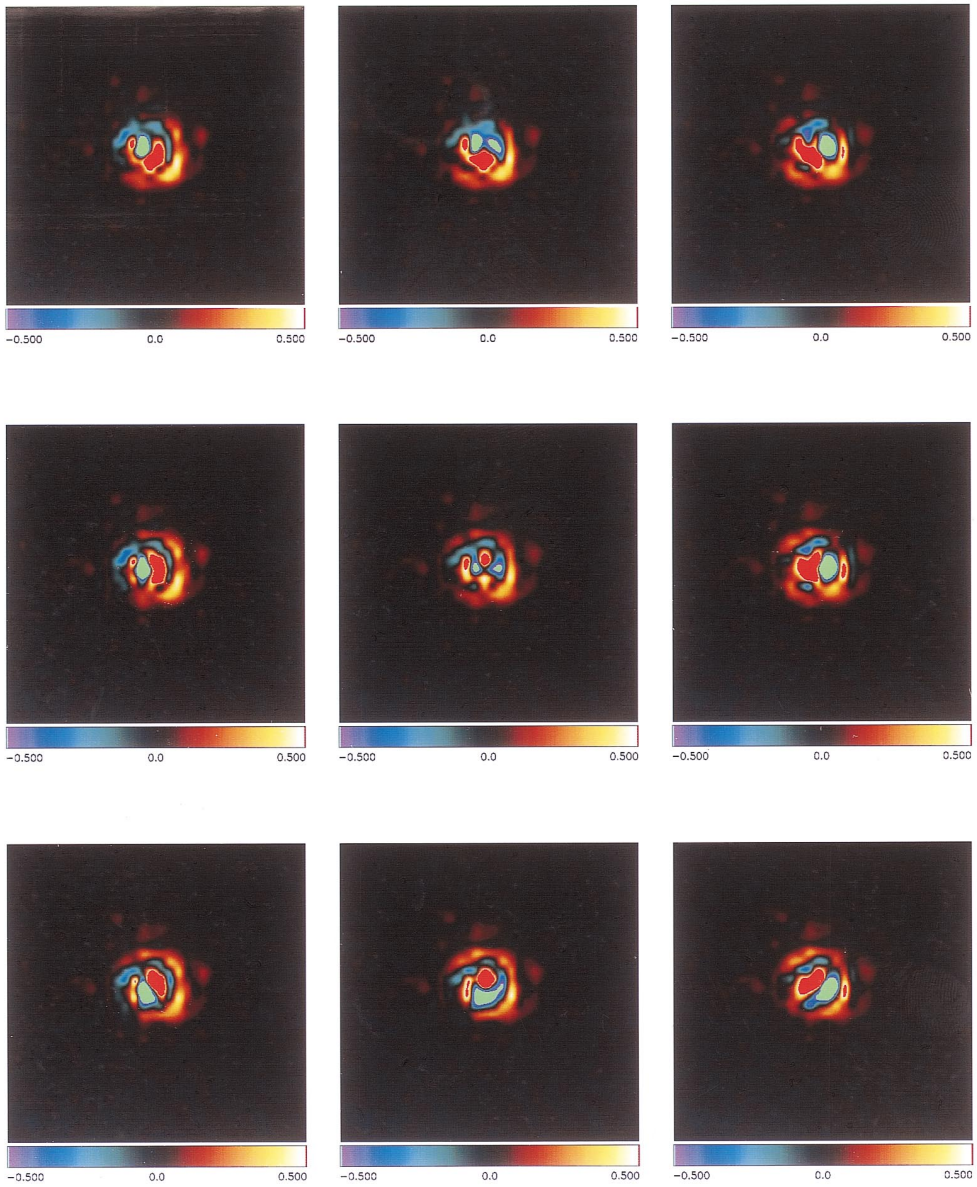

FIG. 18.—Effect of shifting the PSF star by 0.1 pixel in various directions relative to the quasar on the PSF-subtracted noncoronagraphic F160W image. The central panel (*e*) is the optimum minimum-variance solution (same as Fig. 4 [*bottom*]). Top central (*b*) and bottom central (*h*) panels correspond to PSF star shifts of 0.1 pixel in $+y$- and $-y$-directions. Left central (*d*) and right central (*f*) panels correspond to PSF star shifts of 0.1 pixel in $-x$- and $+x$-directions. Top left (*a*), top right (*c*), bottom left (*g*), and bottom right (*i*) panels correspond to PSF star shifts of 0.1 pixel in the top left, top right, bottom left, and bottom right directions, respectively. The large residuals caused by the slight shifts illustrate how well centered the PSF star is with respect to the quasar in the optimum PSF subtraction. The regions shown are 2.″74 × 2.″71 regions around the quasar.

and 88.6 h_{70}^{-1} kpc. These large values make it unlikely for any of these features to be the DLA absorber itself.

If real, the continuum emission knots in object O2 may be highlighting the brightest regions in a companion to the DLA galaxy. The roughly filamentary morphology may indicate an edge-on disk galaxy or a part of a spiral arm. Alternatively, it may suggest individual star-forming subgalactic clumps formed in a filamentary overdense region, similar to the filamentary arrangements of galaxies and subgalactic units found in numerical simulations of structure formation. It is interesting to note that the WFPC2 observations of a $z = 2.811$ DLA by Møller & Warren (1998) also indicate a filamentary arrangement of three bright objects, although on a much larger scale (separation of 21″). The angular separation of their closest object from the quasar was 1.″17, whereas for our features O1 and O2, the angular separations are ≈0.″26 and ≈0.″65, respectively. (We note, however, an important difference between our DLA and the DLA studied by Møller & Warren. The latter has a redshift very close to that of the quasar [$z_{\rm em,CIV} = 2.77$, $z_{\rm em,[OIII]} = 2.788$, and $z_{\rm em,H\alpha} = 2.806$]. Therefore, it is likely to be associated with the quasar and may not be representative of DLA galaxies in general.)

The 1 σ noise levels far away from the quasar are 0.011 ADU s^{-1} pixel^{-1} for our PSF-subtracted noncoronagraphic F160W image and 0.0088 ADU s^{-1} pixel^{-1} for the PSF-subtracted coronagraphic F160W image. These levels translate into 0.024 and 0.019 μJy pixel^{-1}, respectively. The corresponding 1 σ noise equivalent magnitudes for the noncoronagraphic and coronagraphic F160W

images are 26.6 mag pixel^{-1} (21.0 mag arcsec^{-2}) and 26.9 mag pixel^{-1} (21.3 mag arcsec^{-2}), respectively. For comparison, the Hubble Deep Field F160W images had a 1 σ noise level of 1.22×10^{-9} Jy per camera 3 pixel (Thompson et al. 1999). Thus, for the field galaxies far from the quasar in the PSF-subtracted F160W observations, our images are about 5.1–5.4 mag less deep than the Hubble Deep Field images.[5]

Our images do not show any objects other than object O2 in the close vicinity of the DLA. From the galaxy number count–magnitude relation based on deep NICMOS images (Yan et al. 1998), about one galaxy is expected for $H < 21$ in the camera 2 field. Thus, our observations are consistent with these predictions within the uncertainties. There is no sign of strong clustering of galaxies around the DLA.

7.3. *Constraints on Star Formation Rate and Dust in DLAs*

It is quite surprising, given the high sensitivity of our observations and the reasonably high rest-frame V-band luminosity of object O1, that O1 shows almost no detectable Hα emission. The lack of significant Hα emission in our images puts fairly tight constraints on the star formation rate in the DLA toward LBQS 1210+1731, i.e., a 3 σ upper limit of 4.0 h_{70}^{-2} $M_\odot$ yr^{-1} for $q_0 = 0.5$, if no dust is assumed. This is by far the most severe existing constraint on the SFR in high-z DLAs. For comparison, the near-IR spectroscopic survey of Bunker et al. (1999), aimed at detecting Hα from DLAs, gave typical upper limits of ≈ 15 $M_\odot$ yr^{-1}, for $q_0 = 0.5$ and $H_0 = 70$ km s^{-1} Mpc^{-1}. In Figure 19, we compare the result from our data (*filled triangle*) with the 3 σ upper limits from Bunker et al. (1999) (*open triangles*). Our limit on the SFR marks an improvement by a factor of 3 over the tightest constraints of Bunker et al. (1999) on the SFR in DLA galaxies. The curve in Figure 19 shows the predicted average SFR(z) in a DLA expected if DLAs are protodisks, as derived by Bunker et al. (1999) using the closed-box model of Pei & Fall (1995) for the global star formation rate. It is clear that our upper limit on the SFR is much lower than the predicted value at $z = 1.89$. We note that the low SFR estimated here is consistent with the result of Djorgovski (1997), who reported an SFR of ≈ 0.7 $M_\odot$ yr^{-1} in the $z = 4.1$ DLA toward DMS 2247−0209, on the basis of a weak Lyα emission line (assuming no dust extinction). (We note, however, that our limit is less sensitive to dust extinction uncertainties owing to the use of Hα rather than Lyα emission.)

In principle, the lack of detectable Hα emission from the DLA could be because of dust extinction, in which case the actual SFR could be higher. In order to reconcile our upper limit of 4.0 $M_\odot$ yr^{-1} for $q_0 = 0.5$, $H_0 = 70$ km s^{-1} Mpc^{-1} with the expectation of the closed-box protodisk model of 38.6 $M_\odot$ yr^{-1}, an optical depth $\tau_{0.66\mu m} \geq 2.3$ would be required at the rest-frame Hα line if a simple screen of dust in front of the DLA is assumed to extinguish the Hα emission. For extinction curves similar to those in the Milky Way, the Small Magellanic Cloud, or the Large Magellanic Clouds, this would imply $\tau_B \geq 3.4$ at $\lambda_B = 4400$ Å. To have such high extinction, the DLA would be required to have a mean dust-to-gas ratio $k \equiv \tau_B(10^{21}/N_{\rm H\,I}) \geq 8.7$. Even if the H I column density is assumed to be higher by a factor of ~ 3 at the position of O1 compared to the $N_{\rm H\,I}$ detected in the DLA line (since the projected separation of O1 from the quasar would indicate that the DLA absorbing region may be a scale length away from the peak of emission from O1), one still requires a mean dust-to-gas ratio $k \gtrsim 3$. This is much higher than the mean dust-to-gas ratio of 0.8 for the Milky Way, or the typical value of ~ 0.03–0.1 for the DLA galaxies, suggested by observations of background quasar reddening and heavy-element depletions (see, e.g., Pei et al. 1991; Pettini et al. 1997, and references therein).

It is, however, possible that the dust may be intermingled with the gas very close to the stars in the DLA. However, given the low dust-to-gas ratios seen in DLA absorbers, it is hard to imagine that most of the Lyman-continuum photons could be absorbed even before Hα photons can be produced. Thus, there is a good chance that the lack of Hα emission could be indeed because of low SFR.

In the absence of dust obscuration, it follows from Figure 19 that our results, as well as those of Bunker et al. (1999), indicate SFRs much lower than the expectations of the protodisk model. This together with the compact sizes seen in our images again suggests that the observations do not

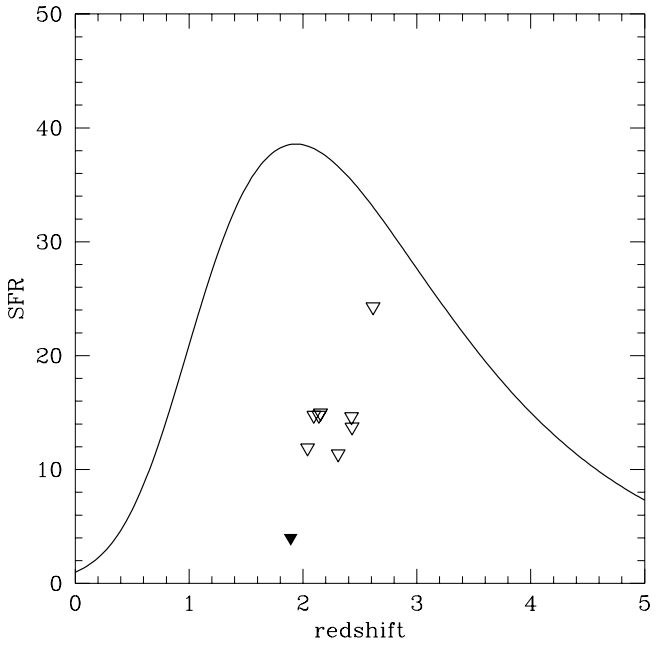

FIG. 19.—Mean star formation rate in DLAs in $M_\odot$ yr^{-1} as a function of redshift, for $q_0 = 0.5$, $H_0 = 70$ km s^{-1} Mpc^{-1}. The filled triangle shows the upper limit from this work, while the unfilled triangles show the limits from Bunker et al. (1999). The curve shows the prediction from a closed-box model applied to protodisk galaxies, as calculated by Bunker et al. (1999). Note that our SFR limit is a factor of 3 improvement over the tightest limits of Bunker et al. (1999) and that most data points are inconsistent with the protodisk model.

[5] Before doing the PSF subtraction, the 1 σ noise levels far away from the quasar are ≈ 0.0046 ADU s^{-1} pixel^{-1} (0.010 μJy pixel^{-1} or 27.6 mag pixel^{-1}) for the noncoronagraphic F160W image and ≈ 0.0084 ADU s^{-1} pixel^{-1} (0.018 μJy pixel^{-1} or 26.9 mag pixel^{-1}) for the coronagraphic F160W image. The process of PSF subtraction decreases the 1 σ deviations by a large factor near the quasar, but increases the noise far away from the quasar. This is because of the use of actually observed PSF star images (with high but finite S/N) for PSF subtraction, which contribute to the noise level. But for reasons mentioned earlier, it is better to use observed PSF star images rather than TINY TIM models to get good matches to the quasar PSF. The higher noise level in the coronagraphic F160W image before PSF subtraction compared to the noncoronagraphic F160W image seems to arise from the use of the target acquisition flat rather than the higher S/N standard flat used for the noncoronagraphic image. In any case, our images both before and after PSF subtraction do not show any field galaxies other than those mentioned above.

agree with the protodisk models. It is possible that O1 is a dwarf galaxy. Star formation in dwarf galaxies is inferred to proceed in bursts separated by quiescent periods lasting up to several Gyr (e.g., Grebel 1998). It may be that we are observing object O1 during such a relatively quiescent stage. It is also possible that O1 is a low surface brightness galaxy, since such galaxies show lower SFR.

7.4. *Alternative Possibilities*

Finally, it is possible that object O1 is not the DLA absorber but that it arises mostly in the quasar host galaxy. We cannot test this possibility further because we do not have narrowband images in filters tuned to $z_{em} = 2.543$. However, we also cannot rule out this possibility. If O1 is in fact the host galaxy of the quasar, then it would have a luminosity (at rest frame 0.45 μm) of $\approx 2.9 \times 10^{10}\ h_{70}^{-2}\ L_{\odot}$ for $q_0 = 0.5$ or $\approx 6.4 \times 10^{10}\ h_{70}^{-2}\ L_{\odot}$ for $q_0 = 0.1$. The images would then suggest that the quasar host is not a large galaxy with or without interactions but rather shows a compact morphology. The strongest feature in the quasar host would then be off center with respect to the quasar nucleus, which has been observed in other quasars. If O1 is in fact the quasar host, then the limits on the luminosity and SFR in the DLA are even more severe than our estimates in §§ 5.1 and 5.2. Conversely, if O1 is the DLA galaxy, then the constraints on the quasar host are more severe than those given above.

It is also possible that O1 is an interloper galaxy at an even lower redshift than the DLA. However, there is no spectroscopic evidence available for this based on the available spectra. Ultraviolet archival spectra with *HST* or *IUE* (which would contain any potential DLA line at a lower redshift) are not available, while the ground-based optical spectra are only medium resolution. We therefore do not consider this possibility further.

8. CONCLUSIONS AND FUTURE WORK

With deep diffraction-limited NICMOS images of LBQS 1210+1731, we have probed regions far closer to the quasar sight line than in most previous studies of high-redshift intervening DLAs. The two objects we report mark the closest detected high-redshift DLA candidates yet to any quasar sight line. Our continuum and Hα images of the $z = 1.89$ DLA toward LBQS 1210+1731 suggest that this DLA is not a big galaxy with a high SFR but may be compact (2–3 h_{70}^{-1} kpc in size), probably consisting of multiple subunits. Assuming no dust extinction of Hα emission, we place a 3 σ upper limit of 4.0 $h_{70}^{-2}\ M_{\odot}\ \mathrm{yr}^{-1}$ on the star formation rate, for $q_0 = 0.5$. Our continuum and Hα observations are consistent with the hierarchical models, in which DLAs arise in several subgalactic clumps or dwarf galaxies, which eventually come together to form the present-day galaxies (see, e.g., York et al. 1986; Matteucci et al. 1997). Indeed, theoretical simulations of merging protogalactic fragments in cold dark matter cosmologies (e.g., Haehnelt, Steinmetz, & Rauch 1998), low surface brightness galaxies (e.g., Jimenez et al. 1999), and collapsing halos with merging clouds (e.g., McDonald & Miralda-Escudé 1999) have also been found to reproduce the observed properties of DLAs (asymmetric line profiles of metal absorption lines, metallicities, H I content, etc.) The small sizes of high-z DLAs suggested by our observations are also consistent with the small sizes of galaxies seen in other independent high-redshift observations, e.g., in the NICMOS Hubble Deep Field observations (Thompson et al. 1999). Together, these observations may be indications that, while star formation had begun long before $z = 2$ resulting in some chemical enrichment, most of the dynamical assembly of galaxies as we know them today occurred more recently, and at $z \sim 2$, the various constituent units were still coming together. However, it cannot be ruled out that the DLA toward LBQS 1210+1731 is a large low surface brightness galaxy with a low SFR, which is below our detection limit even in the F160W image.

We point out that our conclusions are, nevertheless, based on detailed observations of only one high-z DLA. It is quite possible that different DLAs have different rates of evolution because of different physical conditions. Indeed, this is suggested by the large scatter in the metallicity-redshift relation of DLAs (see, e.g., Pettini et al. 1999, and references therein). The NICMOS observations of other DLAs from our sample are currently being analyzed and will help to explore the generality of our conclusions. To improve the statistics of the DLA imaging studies, it is necessary to obtain high spatial resolution near-IR images of more high-redshift DLAs. It would be very valuable to carry out a deeper near-IR imaging survey of more DLAs with *HST*, if the NICMOS cryocooler or the near-IR channel of WFC3 becomes available in the near future. A major advantage of such *HST* observations will be a relatively stable PSF compared to that currently achieved with any ground-based telescope, which is crucial for the detection of DLAs. It will also be of great interest to complement the *HST* observations with observations from adaptive optics systems on large ground-based telescopes. Although these systems will not initially have the relatively stable PSF offered by *HST*, they will be able to achieve even higher spatial resolution and higher imaging sensitivity. Such future space and ground-based observations will provide further insight into the structure and nature of DLA galaxies, and thereby help to constrain theoretical models of the formation and evolution of galaxies.

This project was supported by NASA grant NAG 5-3042 to the NICMOS Instrument Definition Team. It is a pleasure to thank Nicholas Bernstein and Keith Noll for their assistance in the scheduling of our observations. We thank Elizabeth Stobie, Dyer Lytle, Earl O'Neil, Irene Barg, and Anthony Ferro for software and computer support. We also thank Andrew Bunker for making his model star formation rate versus redshift curves available to us ahead of publication.

REFERENCES

Bechtold, J., Elston, R., Yee, H. K. C., Ellingson, E., & Cutri, R. M. 1998, in ASP Conf. Proc. 146, The Young Universe: Galaxy Formation and Evolution at Intermediate and High Redshift, ed. S. D'Odorico, A. Fontana, & E. Giallongo (San Francisco: ASP), 241
Bely, P. 1993, STScI Rep. SESD-93-16
Bunker, A., J., Warren, S. J., Clements, D. L., Williger, G. M., & Hewett, P. C. 1999, MNRAS, 309, 875
Charlot, S., & Fall, S. M. 1991, ApJ, 378, 471
Clements, D. L., et al. 1999, in ASP Conf. Proc. 177, Astrophysics with Infrared Surveys: A Prelude to SIRTF, ed. M. Bicay, R. M. Cutri, & B. F. Madore (San Francisco: ASP), 112
Djorgovski, S. G. 1997, in Proc. IAP Colloq. 13, Structure and Evolution of the IGM from QSO Absorption Line Systems, ed. P. Petitjean & S. Charlot (Paris: Editions Frontières), 303

Djorgovski, S. G., Pahre, M. A., Bechtold, J., & Elston, R. 1996, Nature, 382, 234
Elbaz, D., et al. 1998, in 34th Liege Astrophysics Colloq., The Next Generation Space Telescope: Science Drivers and Technological Challenges, ed. B. Kaldeich-Schurmann (Noordwijk: ESA), 47
Grebel, E. K. 1998, preprint (astro-ph/9806191)
Haehnelt, M., Steinmetz, M., & Rauch, M. 1998, ApJ, 495, 647
Hershey, J. L. 1998, STScI Rep. SESD-97-01, Ver. 2.0
Hershey, J. L., & Mitchell, D. 1998, STScI Rep. (Baltimore: STScI)[6]
Hewett, P. C., Foltz, C. B., & Chaffee, F. H. 1995, AJ, 109, 1498
Hunstead, R. W., Pettini, M., & Fletcher, A. B. 1990, ApJ, 365, 23
Jedamzik, K., & Prochaska, J. X. 1998, MNRAS, 296, 430
Jimenez, R., Bowen, D. V., & Matteucci, F. 1999, ApJ, 514, L83
Kennicutt, R. C. 1983, ApJ, 272, 54
Krist, J., & Hook, R. 1997, The TINY TIM Users's Guide, Ver. 4.4 (Baltimore: STScI)[7]
Kulkarni, V. P., Bechtold, J., Ge, J., & Jannuzi, B. T. 1999, in ASP Conf. Ser. 193, The Hy-Redshift Universe: Galaxy Formation and Evolution at High Redshift, ed. A. J. Bunker & W. J. M. van Breugel (San Francisco: ASP), 603
Kulkarni, V. P., Fall, S. M., & Truran, J. W. 1997, ApJ, 484, L7
Le Brun, V., Bergeron, J., Boisse, P., & Deharveng, J.-M. 1997, A&A, 321, 733
Lowenthal, J. D., Hogan, C. J., Green, R. F., Woodgate, B. E., Caulet, A., Brown, L., & Bechtold, J. 1995, ApJ, 451, 484
Lowrance, P., et al. 1998, in NICMOS and the VLT, ed. W. Freudling & R. Hook (Garching: ESO), 96[8]
Lytle, D., Stobie, E., Ferro, A., & Barg, I. 1999, in ASP Conf. Proc. 172, Astronomical Data Analysis Software and Systems VIII, ed. D. Mehringer, R. L. Plante, & D. A. Roberts (San Francisco: ASP), 445
MacKenty, J. W., Skinner, C., Calzetti, D., & Axon, D. J. 1997, NICMOS Instrument Handbook, Ver. 2.0 (Baltimore: STScI)
Mannucci, F., Thompson, D., Beckwith, S. V. W., & Williger, G. M. 1998, ApJ, 501, L11
Matteucci, F., Molaro, P., & Vladilo, G. 1997, A&A, 321, 45
McDonald, P., & Miralda-Escudé, J. 1999, ApJ, 519, 486
McLeod, B. 1997, in Proc. 1997 *HST* Calibration Workshop, ed. S. Casertano et al. (Baltimore: STScI), 281
McLeod, K., Rieke, G., & Storrie-Lombardi, L. 1999, ApJ, 511, L67
Møller, P., & Warren, S. J. 1998, MNRAS, 299, 661
Møller, P., Warren, S. J., & Fynbo, J. U. 1998, A&A, 330, 19
Pei, Y. C., & Fall, S. M. 1995, ApJ, 454, 69
Pei, Y. C., Fall, S. M., & Bechtold, J. 1991, ApJ, 378, 6
Pettini, M., Ellison, S. L., Steidel, C. C., & Bowen, D. V. 1999, ApJ, 510, 576
Pettini, M., King, D. L., Smith, L. J., & Hunstead, R. W. 1997, ApJ, 478, 536
Prochaska, J. X., & Wolfe, A. M. 1997, ApJ, 487, 73
———. 1998, ApJ, 507, 113
Schneider, G. 1998, in NICMOS and the VLT, ed. W. Freudling & R. Hook (Garching: ESO), 88[9]
Schneider, G., Thompson, R. I., Smith, B. A., & Terrile, R. J. 1998, Proc. SPIE, 3356, 222
Smith, H. E., Cohen, R. D., Burns, J. E., Moore, D. J., & Uchida, B. A. 1989, ApJ, 347, 87
Steidel, C. C., Bowen, D. V., Blades, J. C., & Dickinson, M. 1995a, ApJ, 440, L45
Steidel, C. C., Pettini, M., Dickinson, M., & Persson, S. E. 1995b, AJ, 108, 2046
Storrs, A. 1997, STScI Memo, 1997 November 4 (Baltimore: STScI)[10]
Teplitz, H. I., Malkan, M., & McLean, I. S. 1998, ApJ, 506, 519
Thompson, R. I., Storrie-Lombardi, L. J., Weymann, R. J., Rieke, M. J., Schneider, G., Stobie, E., & Lytle, D. 1999, AJ, 117, 17
Wolfe, A. M., Lanzetta, K. M., Foltz, C. B., & Chaffee, F. H. 1995, ApJ, 454, 698
Wolfe, A. M., Turnshek, D. A., Smith, L. J., & Cohen, R. D. 1986, ApJS, 61, 249
Yan, L., McCarthy, P. J., Storrie-Lombardi, L. J., & Weymann, R. J. 1998, ApJ, 503, L19
York, D. G., Dopita, M., Green, R., & Bechtold, J. 1986, ApJ, 311, 610

[6] Available online at http://www.stsci.edu/ftp/instrument_news/Observatory/focus/ephem.html.

[7] Also available online at http://www.stsci.edu/software/tinytim/tinytim.html.

[8] Also available online at http://ecf.hq.eso.org/nicmos/sardinia/nicmosvlt.html.

[9] Also available online at http://ecf.hq.eso.org/nicmos/sardinia/nicmosvlt.html.

[10] Available online at http://www.stsci.edu/instruments/nicmos/nicmos_advisory_old.html.